Energy Storage Materials 90 (2026) 105353

Contents lists available at ScienceDirect

Energy Storage Materials

journal homepage: www.elsevier.com/locate/ensm

Improving the electro-chemo-mechanical stability of nickel-rich cathodes through tungsten modification for high-performance solid-state batteries

Philip Henkel [a], Ruizhuo Zhang [a], Rajib Sahu [a,b], Christian Kübel [b,c], Jensheer Shamsudeen Seenath [a], Maik Schmitt [a], Ulf-Christian Rauska [d], Celine Röder [d], Fabian Jeschull [d], Jürgen Janek [a,e], Aleksandr Kondrakov [a,f,*], Torsten Brezesinski [a,*]

[a] Battery and Electrochemistry Laboratory (BELLA), Institute of Nanotechnology, Karlsruhe Institute of Technology (KIT), Kaiserstr. 12, 76131, Karlsruhe, Germany
[b] Karlsruhe Nano Micro Facility (KNMFi), Institute of Nanotechnology, Karlsruhe Institute of Technology (KIT), Kaiserstr. 12, 76131, Karlsruhe, Germany
[c] Institute of Materials Science, Technical University Darmstadt (TUDa), Peter-Grünberg-Str. 2, 64287, Darmstadt, Germany
[d] Institute for Applied Materials–Energy Storage Systems, Karlsruhe Institute of Technology (KIT), Kaiserstr. 12, 76131, Karlsruhe, Germany
[e] Institute of Physical Chemistry & Center for Materials Research (ZfM/LaMa), Justus-Liebig-University Giessen, Heinrich-Buff-Ring 17, 35392, Giessen, Germany
[f] BASF SE, Carl-Bosch-Str. 38, 67056, Ludwigshafen, Germany

ARTICLE INFO

Keywords:
All-solid-state battery
Ni-rich cathode
Doping
Thiophosphate solid electrolyte
Electro-chemo-mechanical degradation

ABSTRACT

$LiNiO_2$ represents the Co-free endmember of the layered Ni-rich oxide family and offers the highest practical capacity (energy density) among this class of cathode active materials (CAMs). However, its implementation in thiophosphate-based solid-state batteries is hampered by structural instability and interfacial degradation, particularly at high states of charge. Tungsten incorporation has been identified as a promising strategy to overcome these limitations; proven benefits include reduced particle fracture and improved capacity retention. In the present work, we systematically investigate a wetness impregnation approach applied at the precursor stage to achieve uniform tungsten distribution throughout the bulk and along the grain boundaries. Differential capacity analysis, electron microscopy, electrochemical impedance spectroscopy combined with distribution of relaxation times analysis, X-ray photoelectron spectroscopy, and *in situ* gas analysis collectively show that electro-chemo-mechanical degradation is mitigated during cycling. Taken together, these findings establish tungsten incorporation via precursor impregnation as an effective and scalable route to stabilizing Ni-rich cathodes, with direct implications for the development of high-performance, Co-free CAMs for solid-state battery applications.

1. Introduction

Solid-state batteries (SSBs) using inorganic solid electrolytes (SEs) are widely regarded as a promising alternative to conventional lithium-ion batteries (LIBs) for application in electric vehicles (EVs) [1,2]. Apart from enhanced safety and the potential for higher energy densities, the cell design of SSBs can be simplified and optimized for high-throughput production [3–5]. Thiophosphate-based SEs, such as argyrodite Li_6PS_5Cl (LPSCl), are among the most promising candidates for SSB systems due to their high ionic conductivity at room temperature and favorable mechanical compliance, which enables intimate solid-solid contact in composite electrodes [6,7]. However, their limited electrochemical stability and high reactivity toward layered oxide cathode active materials (CAMs) remain major challenges [8–10].

Among layered cathodes, $LiNiO_2$ (LNO) represents the Co-free endmember of the Ni-rich family and is highly attractive from cost and sustainability perspectives. Stoichiometric LNO offers a high theoretical specific capacity of 275 mAh/g and an average operating potential of about 3.8 V vs. Li^+/Li, making it a prime candidate for high-energy-density batteries [11–13]. In practice, LNO suffers both from major first-cycle capacity loss and from pronounced capacity fading during cycling, which is commonly attributed to kinetic limitations and intrinsic structural instabilities [13–15]. This kind of degradation is linked to the formation of a resistive rocksalt (NiO)-type layer at the surface (grain boundaries) and the presence of antisite defects, most notably Ni^{2+} occupying lithium sites ($Ni_{Li}^{\bullet}$), which hinders ion diffusion [14,16–18]. Furthermore, LNO cathodes undergo a detrimental H2-H3 phase transition during deep (de)lithiation, accompanied by large

* Corresponding authors.
E-mail addresses: aleksandr.kondrakov@basf.com (A. Kondrakov), torsten.brezesinski@kit.edu (T. Brezesinski).

https://doi.org/10.1016/j.ensm.2026.105353
Received 30 April 2026; Received in revised form 14 June 2026; Accepted 2 July 2026
Available online 3 July 2026

anisotropic volume changes [19–21]. The resulting mechanical stresses promote microcrack formation and the progressive deterioration of structural integrity, leading to contact loss and interfacial delamination [22–25]. LNO is also intrinsically prone to cation disordering due to the similar ionic radii of Li^{+} ($r = 0.76$ Å) and Ni^{2+} ($r = 0.69$ Å), leading to partial intermixing even under near-stoichiometric synthesis conditions [16,20,26,27]. While moderate lithium excess can suppress point-defect formation, it often generates residual lithium-containing species that increase interfacial resistance [13,28,29]. Consequently, mitigating adverse phase transitions and stabilizing the particle structure/morphology are key requirements for unlocking the full potential of LNO.

High-valence elemental doping has emerged as an effective strategy to address these challenges [30–33]. In particular, tungsten doping has been reported to effectively improve structural integrity and cycling stability [34–37]. While some reports suggest that tungsten occupies transition-metal sites in the lattice due to its comparable ionic radius (W^{6+}, $r = 0.60$ Å) to Ni^{3+} ($r = 0.56$ Å), it is often found as an ionically conductive Li–W–O secondary phase or segregated at grain boundaries [35–42]. Such intergranular enrichment hinders migration along/across the grain boundaries and suppresses primary-particle coarsening, thereby reducing microcrack formation and alleviating electro-chemo-mechanical degradation [30,32,42,43].

Herein, we report an incipient wetness impregnation strategy applied to $Ni(OH)_2$ and NiO precursor CAMs (pCAMs) using a tungsten-containing solution, followed by calcination in the presence of a lithium source to obtain tungsten-modified LNO, referred to as W-LNO—$Ni(OH)_2$–5% and W-LNO—NiO–5%, respectively, in the following. By combining detailed microstructural characterization with chemical, electrochemical, and gas analyses, the effects of tungsten impregnation on particle morphology, structural stability, and cycling performance are systematically elucidated. The cyclability of the materials is

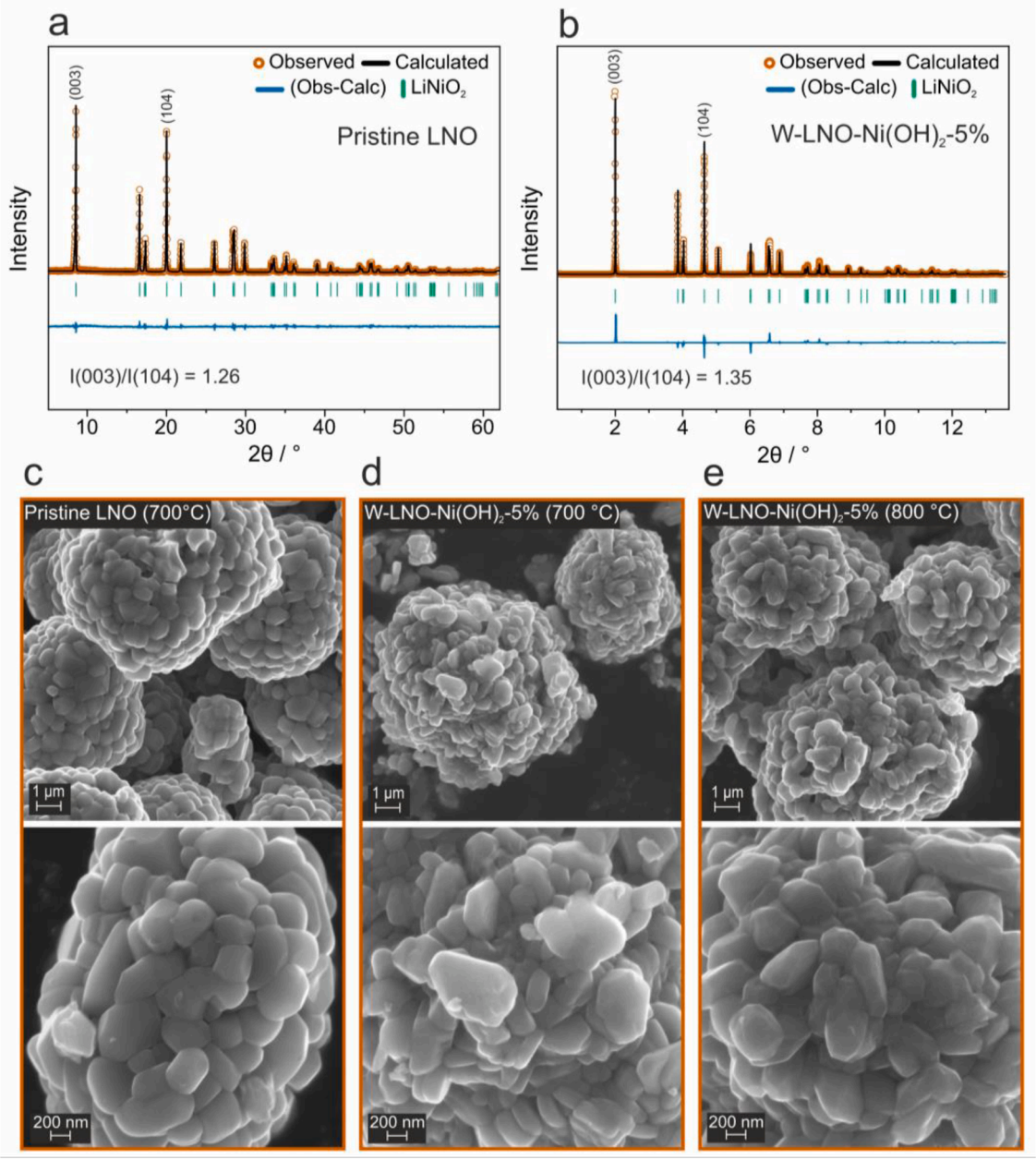

Fig. 1. (a) Rietveld refinement of PXRD data collected from pristine LNO. (b) Rietveld refinement of SXRD data collected from W-LNO—$Ni(OH)_2$–5%. Top-view SEM images at different magnifications of (c) pristine LNO calcined at 700 °C, (d) W-LNO—$Ni(OH)_2$–5% calcined at 700 °C, and (e) W-LNO—$Ni(OH)_2$–5% calcined at 800 °C.

evaluated in two distinct cell environments, namely conventional LIBs and thiophosphate-based SSBs, to assess the universality of the stabilization effect. *Post-mortem* investigations provide further insights into the electro-chemo-mechanical behavior.

2. Results and discussion

For the incipient wetness impregnation, a WCl_6 solution was applied to the pCAM, namely $Ni(OH)_2$ or its dehydrated form (NiO) after heating at 400 °C. In this process, 1.0 wt.% WCl_6 was used [relative to 2 g of $Ni(OH)_2$], which corresponds to 0.5 wt.% elemental tungsten or 0.6 wt.% WO_3. Notably, this initial concentration accounts for ~1.0 wt.% relative to the final LNO. Using a minimal solvent volume leverages capillary forces to ensure proper surface wetting and even distribution of tungsten species [11,31,44–48]. After drying, $LiOH{\cdot}H_2O$ was added in a 5% excess relative to Ni, and the mixture was heated under controlled conditions to obtain tungsten-modified LNO. Unless otherwise specified, W-LNO—$Ni(OH)_2$–5% refers hereinafter to the material synthesized using 1.0 wt.% WCl_6 and calcined at 800 °C. Of note, 3% lithium excess was also tested for samples made from NiO as pCAM (see below). Because Li–W–O species, such as Li_2WO_4, typically begin forming above 600 °C and reach maximum crystallinity above 700 °C, a calcination temperature of 800 °C was selected, aiming at a well-developed microstructure [39,49]. In contrast, pristine LNO was synthesized at 700 °C, as higher calcination temperatures are known to promote lithium loss and primary-particle coarsening, thereby negatively affecting performance [13,50,51].

The crystal structure of both pristine LNO and W-LNO—$Ni(OH)_2$–5% was probed using powder X-ray diffraction (PXRD), synchrotron X-ray diffraction (SXRD), and Rietveld analysis. As shown in Fig. 1**a** and **b**, both CAMs exhibit a rhombohedral α-$NaFeO_2$ structure with space group $R\bar{3}m$, suggesting that the layered framework is preserved upon modification with tungsten. No distinct impurity reflections were observed, indicating that any possible secondary phases are below the instrumental detection limit, which is consistent with previous reports on related tungsten-modified (Ni-rich) cathodes [18,49,52].

The structural ordering in LNO is governed by the ionic radii of Li^+ and Ni^{2+}/Ni^{3+}. Because Li^+ and Ni^{2+} are similar in size, partial cation exchange between the lithium and transition-metal sites is thermodynamically favored, resulting in the intrinsic formation of off-stoichiometric $Li_{1-z}Ni_{1+z}O_2$ [18,53,54]. Here, a 5% excess of lithium was used in the synthesis, which is generally expected to suppress the formation of $Ni^{\bullet}_{Li}$ point defects by providing a lithium-rich environment and compensating for lithium loss (volatilization) at elevated temperatures [20,55,56]. Indeed, for pristine LNO, a Li^+/Ni^{2+} mixing of ~1.5% was determined, as indicated in **Table S1**, matching observations by Kurzhals *et al.* for similar synthesis conditions [20]. Upon introducing W^{6+}, it increased significantly to ~6.7% in W-LNO—$Ni(OH)_2$–5%. This is attributed to the fact that high-valence tungsten induces partial reduction of Ni^{3+} to Ni^{2+} to maintain charge neutrality, thus promoting nickel migration into the lithium sites and increasing the unit-cell volume [36]. Interestingly, despite the higher degree of cation disorder, W-LNO—$Ni(OH)_2$–5% exhibited a higher $I(003)/I(104)$ ratio (1.35) than the pristine LNO (1.26). For the latter material, a higher ratio typically indicates superior layering (ordering). However, in tungsten-modified systems, the increased Ni^{2+} fraction and the potential formation of local rocksalt-like environments can alter the intensity of the 104 reflection, making this ratio less directly comparable to the pristine material [57].

The scanning electron microscopy (SEM) images in Fig. 1**c**–**e** reveal that W-LNO—$Ni(OH)_2$–5% calcined at 700 or 800 °C shows fine primary particles, similar to those of the pristine LNO synthesized at 700 °C. This stabilization is consistent with the segregation of high-valence dopants at the grain boundaries. The enrichment exerts a kinetic pinning effect that delays the coarsening of primary particles, even at elevated temperatures [36,37]. The subtle morphological differences observed between W-LNO—$Ni(OH)_2$–5% calcined at 700 and 800 °C likely relate to the segregation of Li–W–O and/or W–O species. At 800 °C, full crystallization of these phases creates a more continuous and structurally defined intergranular layer, resulting in a more uniform surface morphology [39].

The results from energy-dispersive X-ray (EDX) spectroscopy mapping in **Figure S1a** and **b** confirm the presence of tungsten in both W-LNO—$Ni(OH)_2$–5% samples. The W $K_{\alpha1}$ signals spatially coincide with the Ni- and O-containing regions, suggesting that tungsten has been successfully incorporated into the LNO particles.

High-angle annular dark-field scanning transmission electron microscopy (HAADF STEM) combined with EDX spectroscopy was used to elucidate the spatial distribution of tungsten and its correlation with the local microstructure of W-LNO—$Ni(OH)_2$–5%. As shown in Fig. 2**a**, the elemental mapping indicated a depletion of nickel at the grain boundaries and enrichment of tungsten. However, due to the low dopant concentration, it is difficult to locate tungsten-rich clusters. Normally, W^{6+} enriches locally in the formation of Li–W–O species near intergranular regions, a characteristic feature of high-valence dopant chemistry that explains the limited solubility in the layered structure [58].

Chemical identification was further pursued using electron energy-loss spectroscopy (EELS). The spectrum in Fig. 2**b** shows a minor peak at 595.5 eV, which can be assigned to the W N_1-edge, while characteristic peaks for oxygen (529.3 eV) and the Ni L_2/L_3-edges (854.8/872.2 eV) are clearly resolved. Notably, the major absorptions for tungsten (M_4 and M_5) are situated in an extended energy loss range that exceeds the instrumental detection limit due to poor signal-to-noise ratio. Therefore, a definitive conclusion regarding the exact oxidation state of tungsten cannot be drawn solely from the EELS data. This is further corroborated by the EDX spectrum in **Figure S2a**, which shows the W M-edge; the W L-edges are nevertheless obscured by the high-intensity Ni K-edge signals.

High-resolution STEM (HR-STEM) imaging revealed a distinct structural gradient (Fig. 2**c**), transitioning from a well-ordered layered phase toward a rocksalt-type phase. In this sample, the strongly increased Li^+/Ni^{2+} mixing induced by tungsten incorporation apparently promotes this kind of phase transition. This observation is consistent with the role of W^{6+} in local charge compensation, which can favor cation disorder and destabilize the layering, especially in near-surface regions [36,41]. We note that the aforementioned structural transition was further evidenced in a second region, as shown in **Figure S2b**. Within the ordered domains, the interplanar spacing between the nickel columns was measured to be 4.7 Å. This value is in excellent agreement with the theoretically expected interlayer distance for the (003) planes of rhombohedral LNO, confirming the integrity of the $R\bar{3}m$ framework [14,17]. The corresponding fast Fourier transform (FFT) patterns in Fig. 2**d** and **e** corroborate the coexistence of layered and rocksalt-type phases.

To further elucidate the atomic arrangement within the rocksalt domains, HR-STEM (HAADF) was combined with annular bright-field (ABF) imaging in **Figure S2c** and **d**. Comparison of the HAADF and ABF images showed that the bright spots in the ABF data correspond to the nickel columns and the gray features to oxygen (highlighted by red arrows), thus confirming the presence of oxygen atoms between the nickel columns and providing a more complete picture of the local NiO-type reconstruction. In addition, STEM-EDX analysis of a grain-boundary region is presented in **Figure S2e**. As in the previous observations, a decrease in nickel intensity was found at the grain boundary relative to the oxygen signal, which remained uniform. While tungsten is difficult to localize, the oxygen mapping results suggest that Li–W–O and/or W–O species likely form at these interfaces. The associated EDX spectrum is similar to that shown in **Figure S2a**, exhibiting a clear W M-edge while the L-edges are overlapped by the Ni K-edge signals. Although a definitive local enrichment is difficult to visualize by TEM alone, the observed inhibition of primary particle growth at elevated

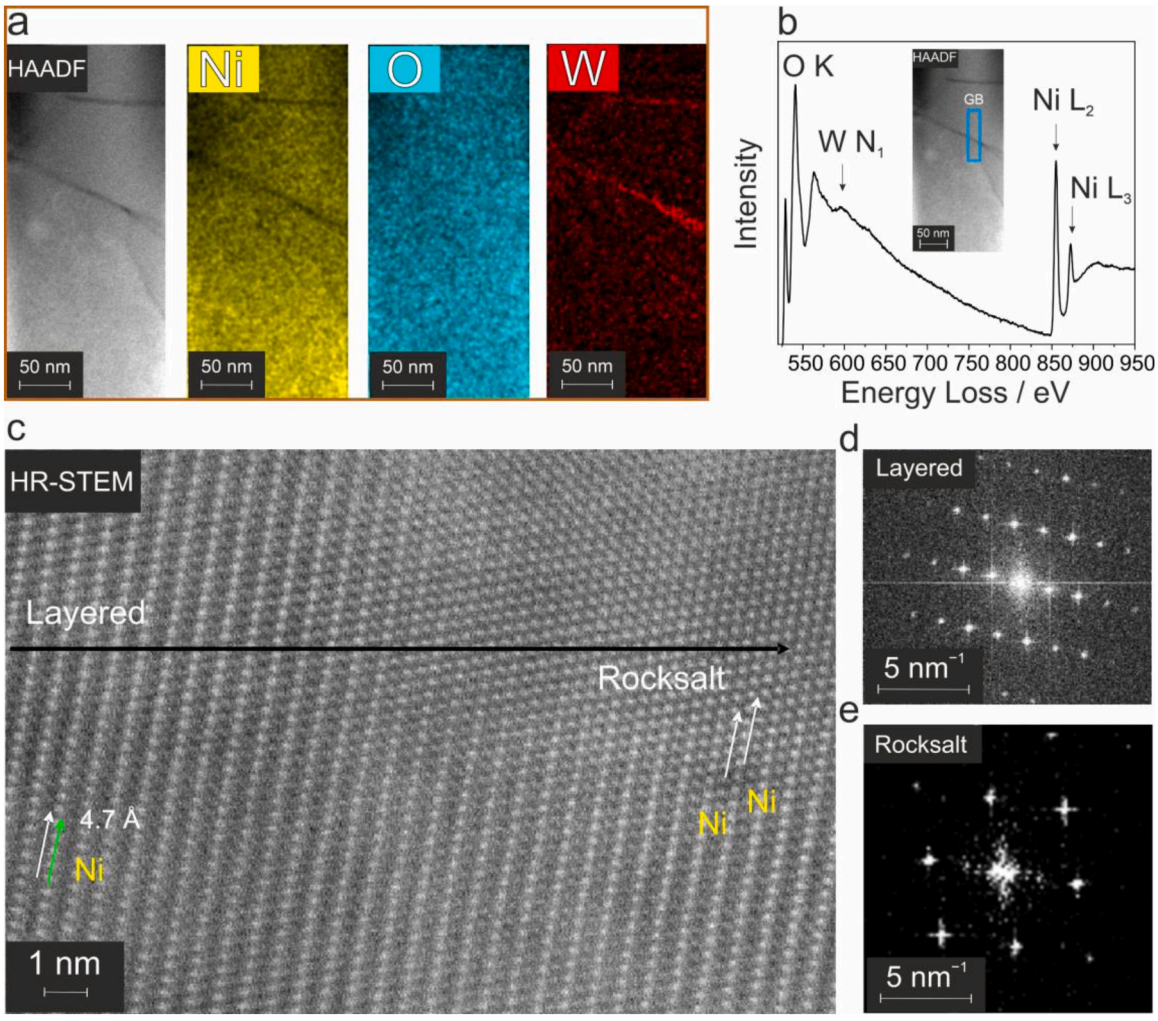

Fig. 2. (a) HAADF image of W-LNO—$Ni(OH)_2$–5% and corresponding results from elemental mapping. (b) EELS spectrum taken from a grain-boundary region, as indicated in the inset. (c) HR-STEM (HAADF) image showing the transition from layered to rocksalt-type phase and (d, e) corresponding FFT patterns.

temperatures is a clear indication of the segregation of tungsten species (e.g. as Li_2WO_4) at the grain boundaries, where they contribute to the stabilization of the microstructure.

The electrochemical performance was first evaluated in LIBs (cathodes with 94% CAM and ~9 mg_{CAM}/cm^2 areal loading) using coin cells with a lithium-metal counter electrode (25 °C, 3.0–4.3 V vs. Li^+/Li). However, prior to comprehensive electrochemical characterization, a systematic screening of synthesis parameters was performed in SSBs to identify the optimal calcination temperature and tungsten content for the modified samples. First, pristine LNO was calcined at 700 and 800 °C and evaluated over 100 cycles at 0.2C, as shown in **Figure S3**. The CAM synthesized at 800 °C delivered a significantly lower initial specific discharge capacity of 146 mAh/g at 0.1C (122 mAh/g after 100 cycles) compared to its 700 °C counterpart, achieving 191 mAh/g in the first cycle and retaining 153 mAh/g, likely due to increased cation mixing and/or particle coarsening at the higher calcination temperature. Interestingly, the tungsten-modified CAMs showed an opposite trend (**Figure S4a** and **b**). Among these, W-LNO—$Ni(OH)_2$–5% (800 °C) achieved the highest initial specific discharge capacity of 209 mAh/g, markedly outperforming the samples heated at 750 and 700 °C, which only delivered 175 and 163 mAh/g, respectively. This superior performance persisted after 20 cycles, suggesting that the formation of favorable (surface) tungsten species requires calcination temperatures exceeding 750 °C.

To determine the optimal tungsten content, the $Ni(OH)_2$ pCAM was impregnated with 1.0, 1.5, and 2.0 wt.% WCl_6, and the resulting materials, after calcination at 800 °C, were electrochemically tested both in LIBs and SSBs (**Figure S5a** and **b**). In LIBs, W-LNO—$Ni(OH)_2$–5% (1.0 wt.%) was found to deliver an initial specific discharge capacity of 229 mAh/g at 0.05C, with a capacity retention of 73% (relative to the first cycle after battery formation) after 100 cycles at 0.5C (equivalent to 147 mAh/g). While W-LNO—$Ni(OH)_2$–5% (1.5 wt.%) achieved a higher specific discharge capacity of 242 mAh/g in the first cycle, it exhibited more pronounced fading, also delivering 147 mAh/g after 100 cycles, corresponding to a capacity retention of 70%. W-LNO—$Ni(OH)_2$–5% (2.0 wt.%) delivered the lowest initial specific discharge capacity of 223 mAh/g and retained only 134 mAh/g (70% capacity retention). In comparison, pristine LNO started at 235 mAh/g, but suffered a significant decline in performance and dropped to 133 mAh/g after 100 cycles, corresponding to a capacity retention of only 63%.

In the SSB configuration, W-LNO—$Ni(OH)_2$–5% (1.0 wt.%) exhibited the best overall performance, delivering an initial specific discharge capacity of 209 mAh/g at 0.1C and achieving the highest capacity of 175 mAh/g after 100 cycles at 0.2C. Increased tungsten contents led to relatively fast capacity decay, with W-LNO—$Ni(OH)_2$–5% (1.5 wt.%) and W-LNO—$Ni(OH)_2$–5% (2.0 wt.%) both starting at about 203 mAh/g and fading to 158 and 99 mAh/g, respectively. Interestingly, both W-LNO—$Ni(OH)_2$–5% (1.0 wt.%) and W-LNO—$Ni(OH)_2$–5% (1.5 wt.%) showed a characteristic increase in capacity during the first 40 cycles, rendering capacity retention values less representative. Based on these

results, a tungsten content of 1.0 wt.% and a calcination temperature of 800 °C were selected for further investigations, whereas 700 °C was used for the pristine LNO.

To elucidate the influence of pCAM type and lithium stoichiometry, W-LNO—$Ni(OH)_2$–5%, W-LNO—NiO–5%, and W-LNO—NiO–3% were compared. Of note, the number (percentage) in the labels refers to the excess lithium used in the synthesis, with W-LNO—NiO denoting CAM prepared by impregnating the NiO precursor prior to lithiation, whereas W-LNO—$Ni(OH)_2$ originates from impregnation of the $Ni(OH)_2$ precursor. The first-cycle charge/discharge profiles of LIB coin cells in Fig. 3**a** indicate that tungsten modification has no significant effect on capacity. W-LNO—NiO–5% exhibited the highest initial specific discharge capacity of 236 mAh/g at 0.05C and a first-cycle Coulomb efficiency (CE) of 90%. W-LNO—$Ni(OH)_2$–5% and W-LNO—NiO–3% achieved capacities of 229 and 231 mAh/g, respectively, corresponding to CEs of 87 and 89%. The pristine LNO delivered an initial specific discharge capacity of 233 mAh/g, with a CE of 90%.

The differential capacity (dq/dV) curves for the second cycle in Fig. 3**b** reveal the characteristic H1-M, M-H2, and H2-H3 phase transitions of LNO. Notably, the redox peaks of pristine LNO were slightly shifted to higher potentials compared to the tungsten-modified samples, indicating higher overpotential and slower reaction kinetics, even at an early stage of cycling. The long-term cycling data in Fig. 3**c** highlight the stabilization effect of tungsten. W-LNO—NiO–5% demonstrated the most stable performance at 0.5C, retaining 164 mAh/g after 100 cycles (79% capacity retention). Both W-LNO—$Ni(OH)_2$–5% and W-LNO—NiO–3% showed moderate fading, retaining 145 and 140 mAh/g, respectively, corresponding to capacity retentions of 72 and 70%. As expected, pristine LNO exhibited the most pronounced degradation, retaining only 99 mAh/g after 100 cycles, corresponding to a capacity retention of 52%. The superior stability of W-LNO—NiO–5% may be attributed to its specific precursor morphology. The increased surface roughness and porosity of NiO likely facilitate more effective tungsten incorporation during calcination, thereby improving structural stability.

The evolution of the dq/dV profiles with cycling in Fig. 3**d**–**f** further supports these findings. For pristine LNO, the phase-transition peaks were significantly broadened and shifted to higher potentials by cycle 10, reflecting structural/morphological changes and increasing internal resistance. In contrast, the tungsten-modified CAMs retained well-defined redox features after 30 cycles. This suggests that the incorporation of tungsten helps suppress the irreversibility of the H2-H3 phase transition and mitigate the electro-chemo-mechanical degradation typically associated with layered Ni-rich cathodes.

Electrochemical measurements in the SSB configuration were conducted on pellet-stack cells with LPSCl as the SE. Testing was performed at an operating temperature of 45 °C and under an external pressure of 81 MPa within a voltage window of 2.3–3.7 V vs. In/InLi (equivalent to about 2.9–4.3 V vs. Li^+/Li). The areal loading was slightly higher than in the LIB case (10–11 mg_{CAM}/cm^2). Fig. 4 compares the cycling performance of pristine LNO, W-LNO—$Ni(OH)_2$–5%, W-LNO—NiO–5%, and W-LNO—NiO–3%. In the initial cycle at 0.1C, W-LNO—$Ni(OH)_2$–5% delivered the highest specific discharge capacity of 209 mAh/g, with a CE of 87% (Fig. 4**a**). Both W-LNO—NiO–5% and W-LNO—NiO–3% achieved lower capacities of 200 and 188 mAh/g, respectively, corresponding to first-cycle CEs of 84 and 83%, while the pristine LNO delivered 191 mAh/g and exhibited the lowest CE of 81%. It should be noted that the CE stabilized quickly beyond 99.5% for all samples tested in this work, even in the SSB cells.

The differential capacity curves for the second cycle in Fig. 4**b** reveal fundamental differences in the phase-transition characteristics. Pristine LNO exhibited a sharp peak for the critical H2-H3 transition in the high-voltage range (> 3.5 V vs. In/InLi). This transition is typically associated

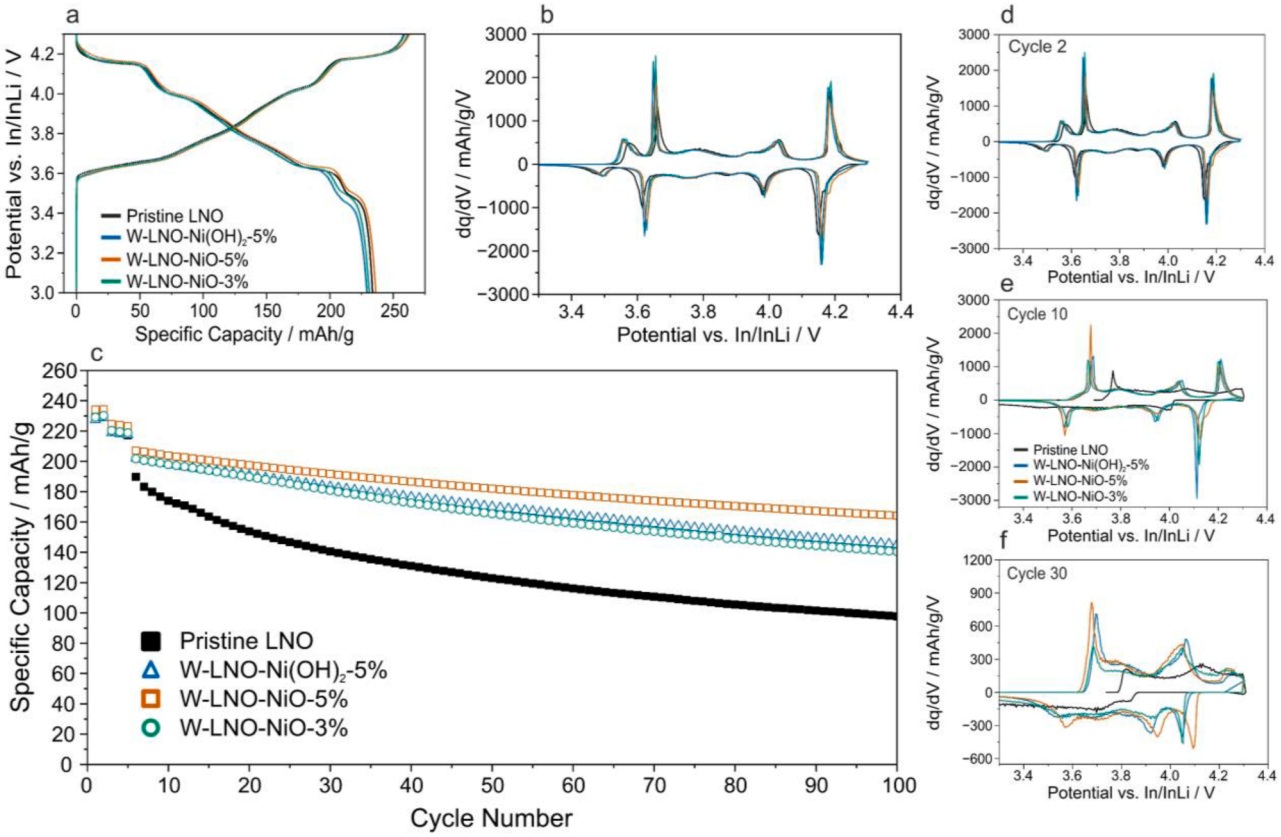

Fig. 3. (a) First-cycle voltage profiles of LIB coin cells using pristine LNO, W-LNO—$Ni(OH)_2$–5%, W-LNO—NiO–5%, or W-LNO—NiO–3% at 25 °C. (b) Second-cycle differential capacity curves. (c) Long-term cycling performance at 0.5C after battery formation, with two cycles at 0.05C and three cycles at 0.1C. Differential capacity curves for cycles (d) 2, (e) 10, and (f) 30.

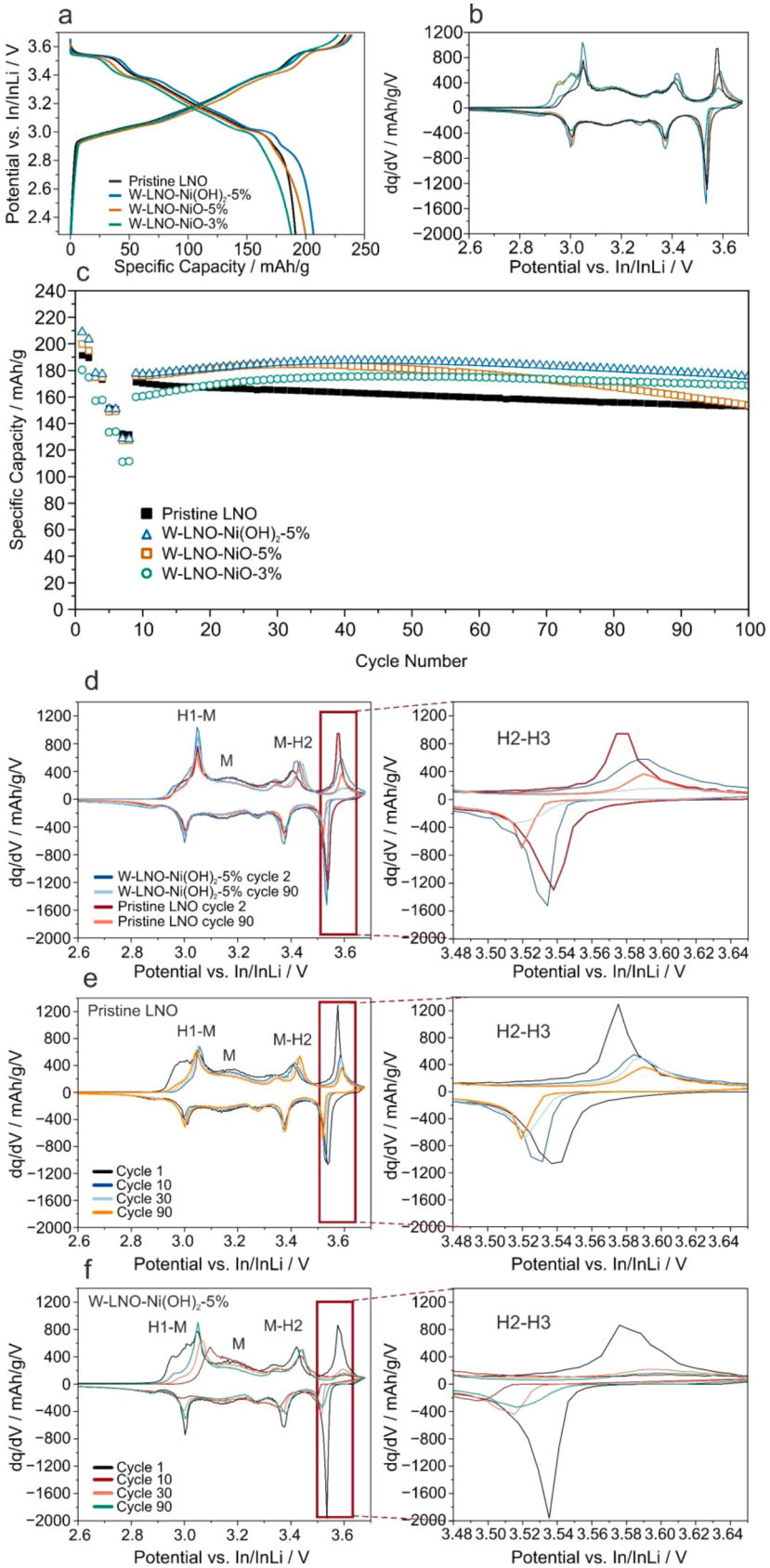

Fig. 4. (a) First-cycle voltage profiles of SSB cells using pristine LNO, W-LNO—$Ni(OH)_2$–5%, W-LNO—NiO–5%, or W-LNO—NiO–3% at 45 °C. (b) Second-cycle differential capacity curves. (c) Rate-performance testing at 0.1C, 0.2C, 0.5C, and 1.0C (two cycles each), followed by long-term cycling at 0.2C. Differential capacity curves comparing (d) cycles 2 and 90 and (e, f) cycles 1, 10, 30, and 90 for pristine LNO and W-LNO—$Ni(OH)_2$–5%. On the right are enlarged views of the H2-H3 phase transition.

with a sudden lattice collapse and distinct anisotropic volume changes, which accelerate chemo-mechanical degradation (particle fracture, interfacial delamination etc.) in the solid-state environment [59,60]. In contrast, the tungsten-modified samples showed a significantly broadened and attenuated H2-H3 peak, reflecting rather a "solid-solution--like" transition. This is presumably due to the increase in Ni^{2+} concentration in the lithium layer induced by tungsten, serving as a kind of structural pillar that helps mitigate the *c*-axis contraction associated with the H2-H3 transition, thereby reducing anisotropic volume changes and mechanical stresses during deep delithiation. A monotonic, detrimental effect of cation mixing on lithium transport is only expected above ~8%, where vacancy depletion and Li-slab compression become dominant [26,36,61].

The long-term cycling data in Fig. 4**c** corroborate these trends, although the performance hierarchy differs from that of the LIB cells. Following the C-rate test, W-LNO—$Ni(OH)_2$–5% continued to perform best, retaining 176 mAh/g after 100 cycles at 0.2C. W-LNO—NiO–5% showed a similar trend up to about 40 cycles, followed by more pronounced fading during prolonged cycling, ending at 153 mAh/g, while W-LNO—NiO–3% exhibited the lowest capacity right after rate capability testing but converged toward a comparable value of 168 mAh/g in the 100th cycle. The pristine LNO revealed a linear decay to 153 mAh/g. Interestingly, W-LNO—$Ni(OH)_2$–5% outperformed W-LNO—NiO–5% in the SSB cells, which may be explained by the differences in precursor morphology. Analogous to the behavior reported for layered Li-rich oxides, where carbonate-derived materials with higher internal porosity benefit from improved electrolyte infiltration and lithium diffusivity, while hydroxide-derived counterparts with more compact particle packing show superior interfacial stability, a similar picture emerges here [62]. The more porous NiO-derived pCAM may facilitate tungsten incorporation and electrolyte accessibility, promoting rate performance in liquid-electrolyte cells, whereas the $Ni(OH)_2$-derived pCAM likely favors a more uniform surface enrichment of tungsten, forming a protective, "coating-like" layer that is beneficial for the sensitive CAM|SE interface in thiophosphate-based SSBs.

A notable feature of the tungsten-modified samples is the gradual increase in capacity between cycle 10 and 40. Fig. 4**d** shows the evolution of the H2-H3 transition for pristine LNO and W-LNO—$Ni(OH)_2$–5%. As mentioned earlier, pristine LNO showed a sharp peak in the second cycle. At cycle 90, this peak clearly lost intensity and broadened, indicating a loss of capacity in the high-voltage range following prolonged SSB operation. W-LNO—$Ni(OH)_2$–5% retained an attenuated peak, even after long-term cycling, suggesting more controlled and better reversible phase transitions. This demonstrates that the tungsten-modified CAM is capable of somewhat mitigating lattice strain in highly delithiated states, thereby minimizing volume variations and the loss of electrochemically active material. The d*q*/d*V* profiles in Fig. 4**e** and **f** further highlight the different degradation pathways. For pristine LNO, the H2-H3 peak progressively diminished in intensity and shifted to higher potentials from cycle 1 to 90, reflecting increasing polarization and impaired kinetics. By contrast, W-LNO—$Ni(OH)_2$–5% showed a significant attenuation of the H2-H3 peak between cycle 1 and cycle 10, followed by stabilization at higher cycle numbers. We observe that the attenuation in the early cycles is at least partially attributable to an increased overpotential induced by the tungsten-containing surface layer, which shifts and broadens the corresponding feature in the d*q*/d*V* profile. The CAM|SE interfacial contact stabilizes over the course of the first few cycles, as described in the section on potentiostatic electrochemical impedance spectroscopy (PEIS). The slightly increased H2-H3-associated charge in cycle 30, compared to cycle 10, is consistent with the observed increase in capacity. This atypical behavior suggests that tungsten-induced microstructural and interfacial stabilization enables partial recovery of reversible lithium storage after C-rate testing.

To better contextualize the electrochemical performance achieved in this work, **Table S2** presents a comparison with Ni-rich cathodes that have been reported in the context of sulfide-based SSBs, including uncoated and coated variants of NCA ($LiNi_xCo_yAl_zO_2$) and NCM ($LiNi_xCo_yMn_zO_2$). Specifically, the initial specific discharge capacity, the first-cycle CE, and the capacity retention after 100 cycles at 0.2C are compared. As is evident, W-LNO—$Ni(OH)_2$–5% performs well in this dataset, delivering one of the highest capacities. However, direct quantitative comparisons between different studies are inherently of limited value, as the cyclability in SSBs depends on a number of experimental parameters beyond the CAM itself, such as operating temperature, loading, applied stack pressure, anode material, and the SE used. These factors influence charge transport, interfacial stability, and usable capacity and must be carefully taken into account when interpreting performance comparisons across different studies.

To further investigate this phenomenon, SSB cells incorporating polymeric binders were evaluated (Fig. 5). For this purpose, composite cathodes containing either polytetrafluoroethylene (PFTE, 0.5 wt.%) or polyisobutylene (PIB, 1.0 wt.%) were produced by dry and wet processing, respectively, and compared with the binder-free powder configuration. In all cases, the areal loading was 10–11 mg_{CAM}/cm^2. The PIB-containing cells achieved a superior initial specific discharge capacity of 223 mAh/g (~2.2 mAh/cm^2) at 0.1C and retained 182 mAh/g (~1.8 mAh/cm^2) after 100 cycles at 0.2C, corresponding to a capacity retention of 92% (relative to the first cycle after rate-capability testing). The PTFE-containing cells achieved 215 mAh/g (~2.4 mAh/cm^2) but suffered from a more pronounced fading during cycling, retaining only 161 mAh/g (~1.8 mAh/cm^2, 82% capacity retention). Both systems delivered stable capacities immediately after C-rate testing, indicating that the presence of a binder ensures improved mechanical integrity and better contact between the particles. The suppression of capacity creep provides mechanistic evidence that this phenomenon is not an intrinsic electrochemical activation of the CAM itself, but rather a consequence of changing interactions between particles in binder-free cells upon cycling. The addition of a binder apparently creates a more robust cathode structure, even before cycling, thus suppressing this kind of "activation" and ensuring consistent long-term performance.

To further elucidate the origin of the enhanced electrochemical performance and the peculiar capacity evolution of the tungsten-modified samples, PEIS analysis was performed (Fig. 6). Impedance spectra were recorded after charging the cells to 3.7 V vs. In/InLi, followed by a 1 h relaxation period under open-circuit voltage (OCV) conditions. This protocol ensures a well-defined (delithiated) state while minimizing the transient contributions of the In/InLi anode in the mid- to low-frequency range, as suggested in the literature [63,64]. The Nyquist plots for SSB cells using pristine LNO, W-LNO—$Ni(OH)_2$–5%, or

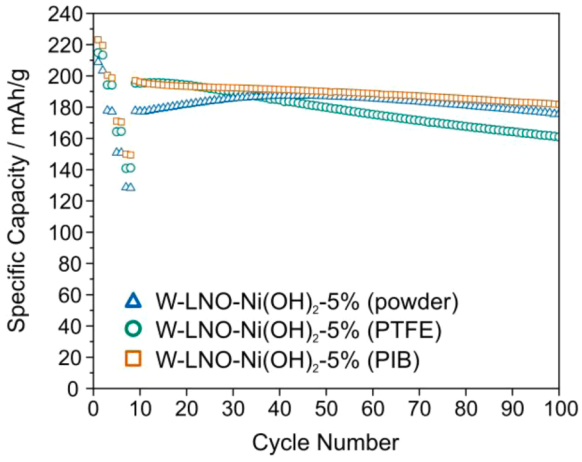

Fig. 5. Rate-performance testing at 0.1C, 0.2C, 0.5C, and 1.0C (two cycles each) of W-LNO—$Ni(OH)_2$–5% in binder-free as well as in PTFE- and PIB-containing SSB cells at 45 °C, followed by long-term cycling at 0.2C.

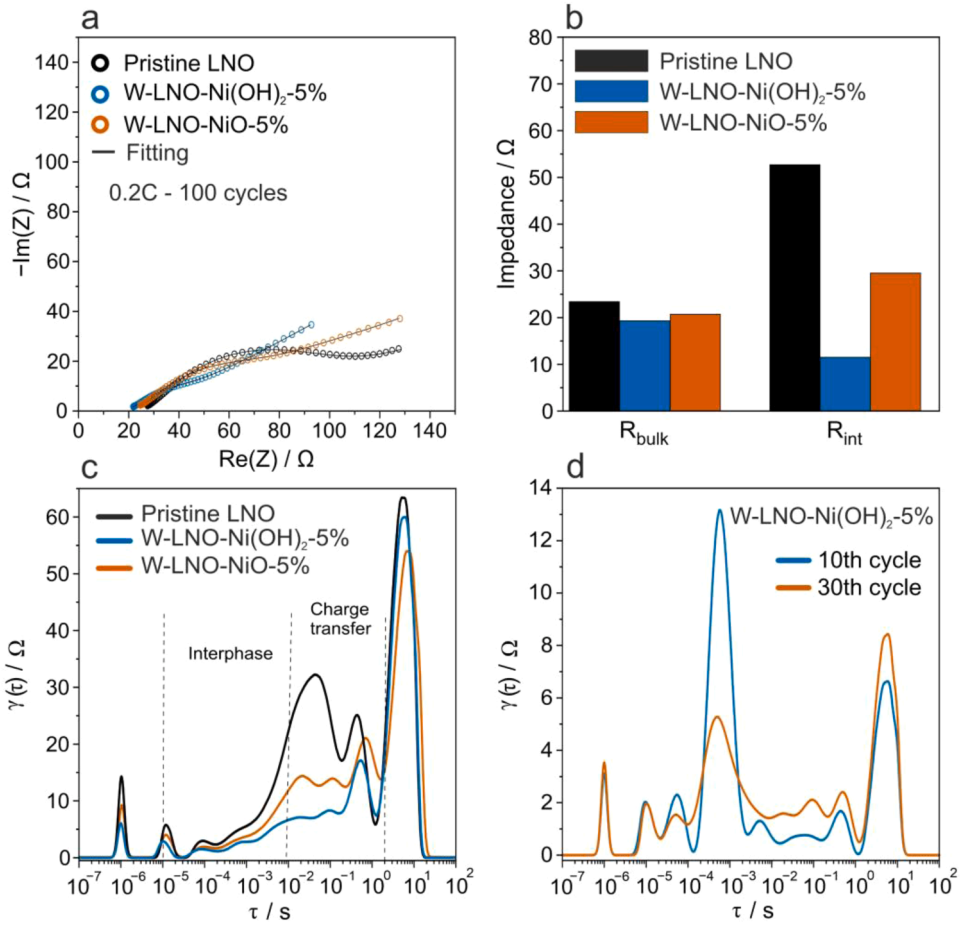

Fig. 6. (a) Nyquist plots of the electrochemical impedance of SSB cells (at the end of charge) using pristine LNO, W-LNO—$Ni(OH)_2$–5%, or W-LNO—NiO–5% after 100 cycles at 0.2C and 45 °C, including ECM fitting. (b) Corresponding R_{bulk} and R_{int} and (c) DRT patterns. (d) DRT patterns of W-LNO—$Ni(OH)_2$–5% for cycles 10 and 30 at the end of charge.

W-LNO—NiO–5% after 100 cycles at 0.2C in Fig. 6**a** show that both tungsten-modified CAMs exhibited a significantly lower impedance than pristine LNO. For quantitative analysis, the Nyquist plots were fitted using an equivalent circuit model (ECM). Details can be found in **Figure S6** and are summarized in **Table S3**. As can be seen from Fig. 6**b**, all samples had a comparable bulk resistance (R_{bulk}) with an average value of 21.1 Ω, while the interfacial resistance (R_{int}) showed major differences. In principle, R_{int} includes contributions from the resistance of the as-formed cathode-electrolyte interphase (CEI) and from charge-transfer processes at both the cathode and anode interfaces [65, 66]. Although it is challenging to distinguish individual electrochemical processes from overlapping semicircles solely through ECM fitting in the frequency domain, the R_{int} value can still provide direct insight into the positive effect of tungsten modification. Specifically, W-LNO—$Ni(OH)_2$–5% showed the lowest R_{int} (12.1 Ω), whereas W-LNO—NiO–5% exhibited a value of 29.5 Ω. In contrast, pristine LNO revealed a drastic increase in R_{int} to 52.7 Ω, indicating a significant deterioration in reaction kinetics and interfacial integrity. This result confirms that the introduction of tungsten effectively limits the increase in interfacial resistance during SSB operation.

To better understand the individual contributions, distribution of relaxation times (DRT) analysis was performed. As shown in Fig. 6**c**, the peaks in the DRT patterns reflect characteristic electrochemical processes. The time constants of interfacial kinetic processes can be divided into two main regions: (i) an intermediate-frequency range with 10^{-5} s $< \tau < 10^{-2}$ s, attributed to the as-formed interphase, and (ii) a medium-to-low-frequency range with 10^{-2} s $< \tau < 1$ s, associated with charge-transfer processes [66,67]. A comparison of the cathodes after 100 cycles (Fig. 6**c**) indicates that the primary cause of interfacial kinetic hindrance lies in the charge-transfer processes in region (ii), with the pristine LNO being most severely affected. Among the tungsten-modified samples, W-LNO—$Ni(OH)_2$–5% exhibits more favorable kinetics than W-LNO—NiO–5%, in good agreement with the ECM-based analysis presented above.

The evolution of DRT peaks for W-LNO—$Ni(OH)_2$–5% during cycling further provides a possible explanation for the observed increase in capacity in the initial cycles. Fig. 6**d** shows a distinct peak in region (i) after 10 cycles, followed by a marked decline by the 30th cycle. This trend is closely linked to the creep behavior discussed above, suggesting progressive interfacial stabilization. We assume that this is due to the fact that the tungsten-containing secondary phases gradually reach a structural equilibrium under the applied external pressure and electrochemical stress. Such a process likely optimizes the lithium and electron transport pathways and improves contact between the CAM and SE particles.

A cross-sectional analysis was then performed using SEM to assess the structural integrity of the cathodes after 100 cycles at 0.2C, as shown in Fig. 7. For pristine LNO (Fig. 7**a**), severe mechanical degradation was evident. Intergranular cracks were clearly distributed throughout the entire secondary particles and extended from the surface deep into their interior. These cracks appeared across multiple length scales, indicating chemo-mechanical fatigue caused by anisotropic lattice strain during (de)lithiation. Such structural disintegration increases the interfacial area for parasitic side reactions with the SE, eventually leading to electrochemical isolation of CAM fragments [68–70]. In contrast, W-LNO—$Ni(OH)_2$–5% (Fig. 7**b**) exhibited significantly improved

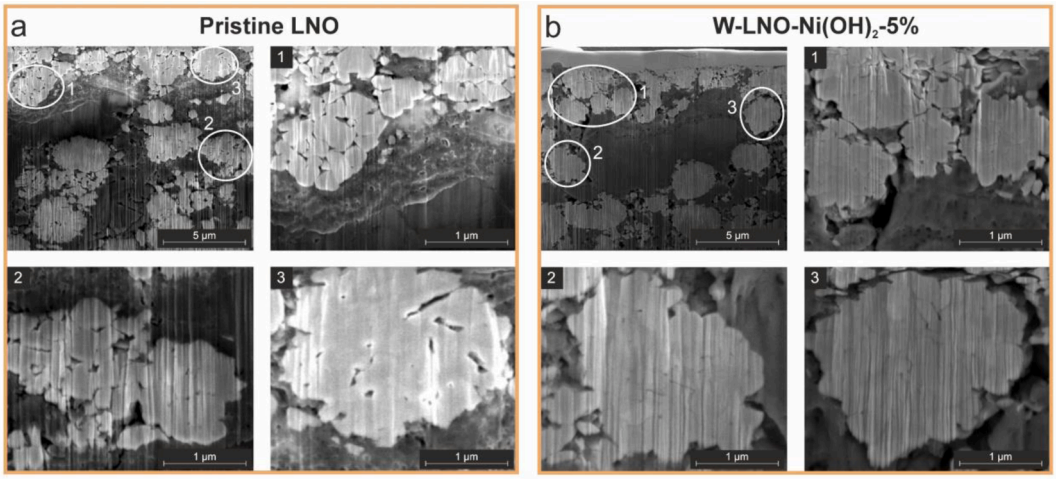

Fig. 7. Cross-sectional SEM images of the composite cathodes after 100 cycles at 0.2C and 45 °C in SSB cells. (a) Pristine LNO and (b) W-LNO—$Ni(OH)_2$–5%.

structural integrity. The secondary particles remained relatively dense, with only a few visible microcracks. Specifically, the mitigation of H2-H3 transition due to tungsten incorporation reduces internal mechanical stresses, thus preserving the intra- and interparticle connectivity as well as the morphological integrity of the cathode.

To further investigate the fracture kinetics, acoustic emission (AE) measurements were performed during cycling of the CAMs in LIB coin cells. AE testing detects transient elastic waves generated by individual structural failure events, such as crack initiation and propagation, providing real-time insight into the mechanical degradation [71–73]. **Figure S7a** and **b** shows voltage profiles alongside the hit rate and cumulative hits. Pristine LNO exhibited intense acoustic activity, particularly in the first three cycles at potentials above ~4.0 V vs. Li^+/Li, which correlates with the H2-H3 transition. Overall, this result suggests mechanical cracking during the initial cycles. In contrast, W-LNO—Ni$(OH)_2$–5% showed significantly fewer acoustic signals throughout the entire cycling period. This reduction in acoustic activity confirms that tungsten modification effectively suppresses chemo-mechanical degradation by stabilizing the crystal lattice and inhibiting crack formation, in agreement with the SEM observations.

X-ray photoelectron spectroscopy (XPS) measurements were also conducted on the cathodes before cycling and after 30 cycles at 0.2C and 45 °C in SSB cells. Fig. 8 shows both normalized P 2p and S 2p core-level spectra and results from quantitative analysis. The complete dataset, including various other core-level regions, is provided in **Figure S8**. In the P 2p region, the spectrum of the non-cycled W-LNO—Ni$(OH)_2$–5% was dominated by the PS_4^{3-} doublet at ~132.0/133.1 eV, characteristic of the argyrodite structure, with only a minor contribution from oxygenated phosphorus (PO_x) species at ~134.5/135.5 eV, as shown in Fig. 8**a** [3,74]. After 30 cycles, the two samples exhibited markedly different spectra, indicating that different interfacial degradation mechanisms occur. For W-LNO—Ni$(OH)_2$–5%, the P 2p spectrum was dominated by phosphorus polysulfide intermediates (P_2S_x) at ~133.5/134.4 eV, which represent the primary (oxidative) decomposition product, while the PS_4^{3-} fraction was strongly diminished. Importantly, this electrochemical degradation pathway does not require the involvement of lattice oxygen from the CAM. In contrast, pristine LNO showed a comparatively lower relative fraction of P_2S_x, while the PO_x contribution was slightly increased. Since the CAM itself is the only available oxygen source in the cathode, the PO_x contribution is a fingerprint of oxygen-driven CAM|SE interfacial degradation, facilitated by the absence of a protective surface layer. Therefore, the formation of oxygenated phosphorus species can be directly attributed to adverse side reactions between CAM and SE [3,9,75]. The S 2p region provides complementary and quantitatively decisive evidence. In the pristine

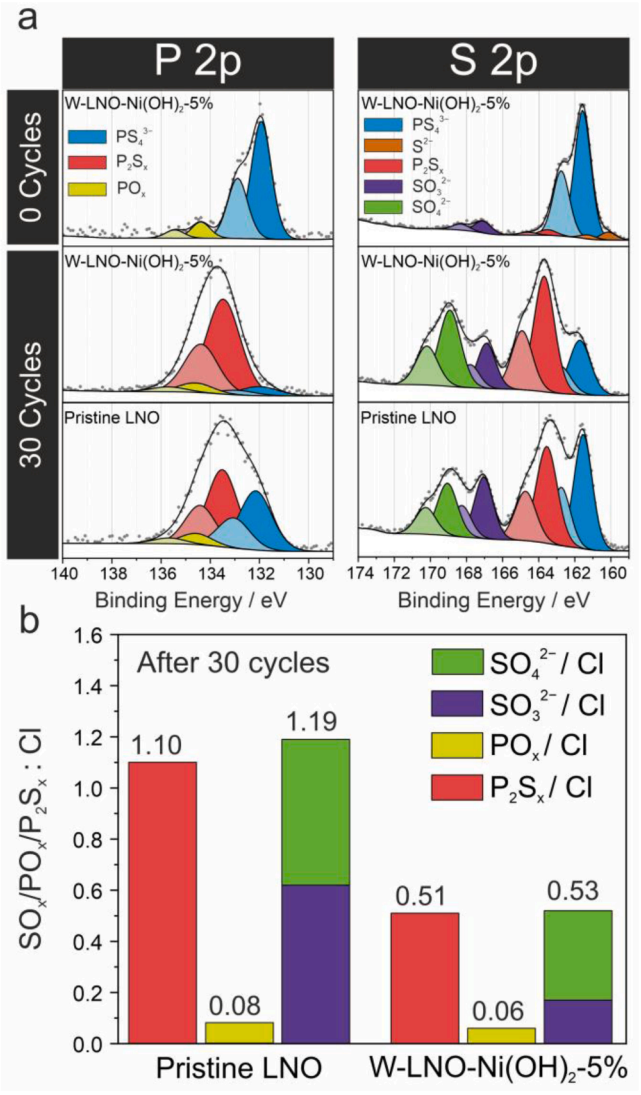

Fig. 8. (a) Normalized XPS detail spectra of the P 2p and S 2p core-level regions for W-LNO—Ni$(OH)_2$–5% prior to cycling (as reference) and after 30 cycles, as well as for pristine LNO after 30 cycles at 0.2C and 45 °C in SSB cells. (b) Corresponding SO_x/Cl, PO_x/Cl, and P_2S_x/Cl ratios determined by quantitative analysis.

state, the spectrum of W-LNO—Ni(OH)$_2$–5% was governed by the PS_4^{3-} doublet at ~161.7/162.9 eV, with only small peaks attributable to P_2S_x species at ~163.5/164.7 eV and negligible contributions from oxygenated sulfur (SO_x) [10,76]. After 30 cycles, sulfate (SO_4^{2-}, ~169.1/170.3 eV) and sulfite (SO_3^{2-}, ~167.2/168.4 eV) species formed in both cathodes, which is consistent with the anodic SE decomposition triggered by reactive oxygen released from the CAM at high degrees of delithiation [65].

To account for differences in interphase thickness between the samples, the SO_x, PO_x, and P_2S_x contributions were normalized to the Cl 2p signal. The latter was chosen since Cl^-, to the best of our knowledge, does not participate in any electrochemical redox reactions [74]. The validity of this approach is supported by the Cl 2p spectra shown in **Figure S8**. After 30 cycles, the Cl 2p peaks retained their characteristic binding energies and line shapes for both pristine LNO and W-LNO—Ni(OH)$_2$–5%, with no signs of the formation of chlorine-containing degradation products. Overall, this normalization is essential because, otherwise, the P 2p spectra might give the impression that there is greater degradation in W-LNO—Ni(OH)$_2$–5% due to the relative suppression of the PS_4^{3-} signal. Regardless, this procedure eliminates the interference caused by signal attenuation due to the growing interphase and allows for a semi-quantitative comparison of the extent of SE oxidation. The resulting ratios are illustrated in Fig. 8**b**. W-LNO—Ni(OH)$_2$–5% exhibited an SO_x/Cl ratio of 0.53, compared to 1.19 for pristine LNO, demonstrating the more vigorous oxygen-driven SE degradation in the case of pristine LNO. The PO_x/Cl ratio of 0.08 for pristine LNO, compared to 0.06 for W-LNO—Ni(OH)$_2$–5%, further corroborates the mitigation of the oxygen-driven reaction pathway for the tungsten-modified sample. Additionally, the P_2S_x/Cl ratio (considering the S 2p spectra) was also significantly higher for pristine LNO (1.10) than for W-LNO—Ni(OH)$_2$–5% (0.51), confirming more pronounced SE decomposition at the pristine LNO|LPSCl interface. It is expected that the higher fraction of oxidized sulfur species will result in a more resistive CEI. This is consistent with the higher interfacial resistance observed in SSB cells using pristine LNO (Fig. 6**b**).

The Ni 2p spectra after 30 cycles in **Figure S8** show the characteristic (multiplet) signatures of Ni^{2+} and Ni^{3+}. For W-LNO—Ni(OH)$_2$–5%, the W 4f region revealed a single doublet with the W $4f_{7/2}$ component located at ~35.5 eV across all cycling states, consistent with W^{6+}, as expected for tungsten in an oxygen-coordination environment [77]. No contributions due to partially reduced tungsten (~33.0 eV) were observed, confirming that the surface species remain chemically and electrochemically stable throughout cycling and do not undergo changes in oxidation state upon contact with the SE.

Finally, differential electrochemical mass spectrometry (DEMS) was used to investigate the outgassing behavior of pristine LNO, W-LNO—Ni(OH)$_2$–5%, and W-LNO—NiO–5% during electrochemical cycling. Gas evolution is a critical degradation pathway in Ni-rich cathodes, particularly at potentials, where extensive delithiation destabilizes the layered structure, triggering lattice oxygen release and parasitic side reactions [78–80]. In SSB systems, intimate contact between CAM and SE further facilitates interfacial degradation [81]. The measurements were conducted using a customized, low-stack-pressure DEMS configuration (without applying external pressure). Consequently, reduced interfacial contact resulted in lower reversible capacities and first-cycle CEs (pristine LNO: 72%, W-LNO—Ni(OH)$_2$–5%: 65%, W-LNO—NiO–5%: 71%) than in the pellet-stack cells described above, as shown in **Figure S9**. Regardless, the DEMS cells were cycled at a rate of 0.05C and at 45 °C to ensure sufficient delithiation, achieving first-cycle specific charge capacities exceeding 210 mAh/g [> 75% state of charge (SOC)].

The evolution of H_2 ($m/z = 2$), O_2 ($m/z = 32$), CO_2 ($m/z = 44$), and SO_2 ($m/z = 64$) was monitored in Fig. 9**a** and **b**, with both pristine LNO and W-LNO—Ni(OH)$_2$–5% limited to a comparable SOC of 77% to enable direct comparison. Hydrogen release was observed primarily at the onset of the first charge cycle for all samples, with 2.5–3.0 µmol/g_{CAM}. This can be attributed to the reduction of trace water [76,81].

Carbon dioxide evolution originates predominantly from the electrochemical oxidation of residual carbonate species on the free surface of CAMs, formed during synthesis and air exposure [79,82]. For pristine LNO and W-LNO—Ni(OH)$_2$–5% (**Figure S10a**), the CO_2 evolution started at about 3.2 V vs. In/InLi (~3.8 V vs. Li^+/Li), followed by a second evolution peak near 3.6 V. The total CO_2 amounts reached about 3.5 µmol/g_{CAM} for pristine LNO and 2.0 µmol/g_{CAM} for W-LNO—Ni(OH)$_2$–5% (**Figure S10a**). In contrast, W-LNO—NiO–5% (**Figure S10b**) and W-LNO—Ni(OH)$_2$–5% (Fig. 9**b**) exhibited a single CO_2 peak with total amounts of only ~0.35 µmol/g_{CAM} and ~4.0 µmol/g_{CAM}, respectively. It is important to note though that the W-LNO—Ni(OH)$_2$–5% data shown in **Figure S10a** and Fig. 9**b** are from different batches. Since residual surface carbonate content depends on exposure to air during handling and processing, batch-to-batch variations in CO_2 evolution,

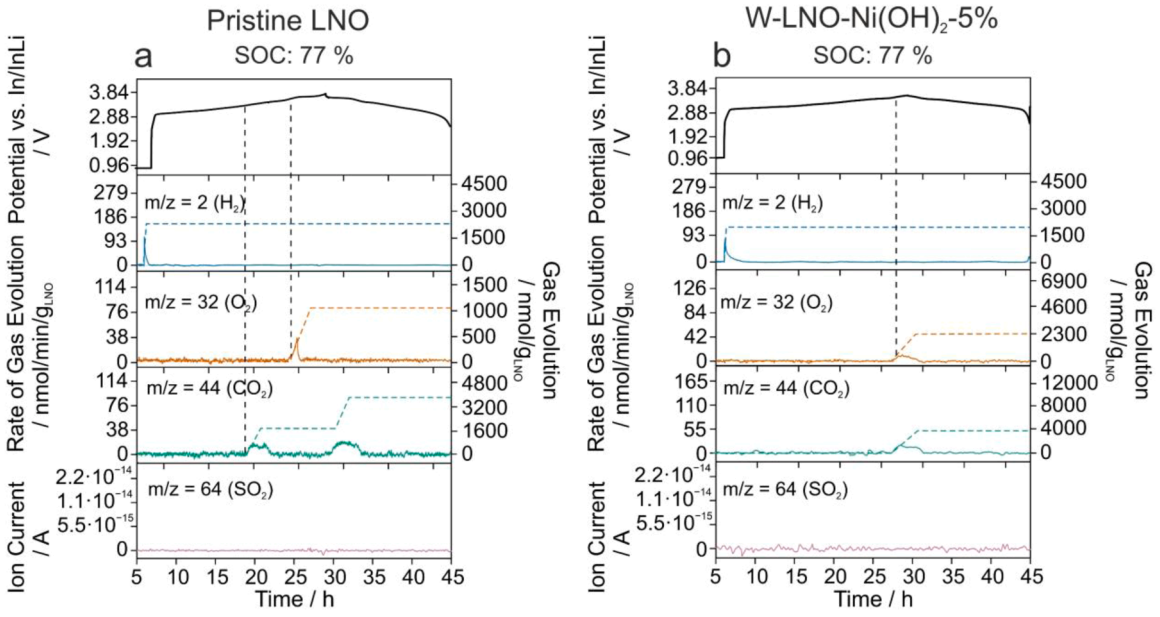

Fig. 9. First-cycle voltage profiles of SSB cells using (a) pristine LNO and (b) W-LNO—Ni(OH)$_2$–5% at 0.05C and 45 °C with time-resolved evolution rates of H_2, O_2, CO_2, and SO_2 and corresponding cumulative amounts from *in situ* gas analysis.

especially in the low-voltage range, are to be expected and do not reflect intrinsic differences in material properties. The two-step CO_2 evolution in the other samples suggests that carbonates exist in distinct chemical environments, at the particle surface and likely also partially confined within grain boundaries, where the release is initiated by particle fracture at high SOC. However, follow-up reactions of released (reactive) lattice oxygen with the carbon additive cannot be fully ruled out. The substantially lower CO_2 evolution observed for W-LNO—NiO–5% highlights the advantage of the NiO-based precursor route, where additional thermal treatment and an altered surface morphology facilitate the removal of residual lithium during synthesis.

Oxygen evolution usually serves as a direct indicator of lattice oxygen loss during deep delithiation of Ni-rich cathodes [12,76]. Pristine LNO showed a single peak at about 3.5 V, coinciding with the onset of structural instability. W-LNO—$Ni(OH)_2$–5% (**Figure S10a**) revealed two peaks at 3.2 and 3.6 V, with the latter reaching its maximum in the discharge cycle, as can be seen in **Figure S11**. The higher cumulative oxygen evolution for W-LNO—$Ni(OH)_2$–5% (~6.0 μmol/g_{CAM}, **Figure S10a**), compared to pristine LNO (~1.0 μmol/g_{CAM}) and W-LNO—NiO–5% (~3.3 μmol/g_{CAM}), is likely due to differences in SOC (83% vs. 77/78%), reflecting improved electrochemical accessibility. A difference in SOC by ~6% can lead to a disproportionate, nonlinear increase in oxygen evolution [12].

Sulfur dioxide evolution, observed exclusively for W-LNO—$Ni(OH)_2$–5% (**Figure S10a**), is due to the decomposition of SE driven by lattice oxygen loss at high SOC. This is confirmed by the slightly delayed onset of SO_2 evolution relative to that of O_2 (**Figure S11**), meaning that the release of lattice oxygen is a key trigger for the subsequent SE degradation [81,83]. When W-LNO—$Ni(OH)_2$–5% is cycled with a charge-capacity limitation (77% SOC, Fig. 9**b**), it exhibits a significantly lower oxygen evolution of ~2.3 μmol/g_{CAM}, and no SO_2 release is detected. This finding supports the assumption that O_2 release increases strongly beyond ~77% SOC and drives the subsequent SO_2 evolution. Since oxygen evolution was not the lowest for W-LNO—$Ni(OH)_2$–5%, it is clear that tungsten modification does not prevent the release of oxygen from the lattice during cycling. It is worth noting that the gas mixture used for calibration did not contain SO_2, which is why only ion currents are reported without quantitative conversion.

Correlating gas evolution with SOC (**Figure S12a–c**) revealed that, for pristine LNO, O_2 release occurs at ~65%. In contrast, W-LNO—$Ni(OH)_2$–5% (cycled to 83% SOC) exhibited a simultaneous onset of CO_2 and O_2 evolution at ~47%. Since the cumulative amount of evolved O_2 was low and the release occurred too early for lattice oxygen loss, it is suggested that oxidative carbonate decomposition is driving it. However, the second signal at ~80% (during discharge) is believed to be directly related to the oxidation of lattice oxygen. The close temporal correlation between the release of O_2 and CO_2 in the tungsten-modified samples further supports the hypothesis that the destabilization of lattice oxygen, accompanied by particle fracture, triggers further decomposition of the carbonate species. Regardless, the data clearly show that O_2 is released first, leading to the subsequent decomposition of LPSCl, which may produce SO_2.

3. Conclusions

In this work, an incipient wetness impregnation strategy was successfully developed to introduce tungsten into $LiNiO_2$ using either $Ni(OH)_2$ or NiO as the precursor cathode active material. This approach enables the controlled incorporation and distribution of tungsten species within the cathode microstructure. Despite the low concentration, which complicates the definitive localization of tungsten, the experimental data suggest a synergistic stabilization mechanism. While XRD confirms partial incorporation into the layered framework, resulting in improved structural robustness and modulated cation mixing, both SEM and STEM primarily indicate surface segregation. This intergranular enrichment likely facilitates the formation of Li–W–O secondary phases, providing a kinetic pinning effect that suppresses primary particle coarsening. Electrochemical testing in both liquid- and solid-electrolyte battery environments demonstrates significantly improved cycling stability and reversibility for the tungsten-modified materials compared to pristine $LiNiO_2$. Notably, tungsten incorporation mitigates the adverse H2-H3 phase transition, which ultimately leads to a more gradual "solid-solution-like" behavior, thereby reducing the accumulation of lattice strain during battery operation. EIS-DRT analysis also reveals that the tungsten-containing interface promotes fast charge-transfer kinetics. Furthermore, the combination of cross-sectional SEM, XPS, and DEMS provides conclusive evidence of reduced degradation.

Overall, tungsten modification effectively mitigates mechanical cracking and oxygen release, thus minimizing adverse side reactions with the solid electrolyte—a factor that is crucial for the stability of thiophosphate-based solid-state batteries. Taken together, the results highlight that tungsten incorporation at the precursor stage is a powerful and scalable strategy for stabilizing Ni-rich cathode active materials. By leveraging synergistic bulk and surface effects, this approach ensures superior structural integrity, which ultimately paves the way for the development of high-performance and potentially sustainable solid-state batteries.

4. Experimental section

4.1. Preparation of pristine LNO

$Ni(OH)_2$ pCAM (4 μm) was provided by BASF SE. $LiOH{\cdot}H_2O$ was added to the pCAM, considering Li:Ni molar ratios of 1.05 and 1.01 for SSBs and LIBs, respectively. The solids were mixed using a laboratory blender (Kinematica AG) and then transferred to a ceramic crucible. The calcination conditions were 4 h at 400 °C and 6 h at 700 or 800 °C, with a heating rate of 3 °C/min, in an O_2 atmosphere (4 L/h). Subsequently, sieving to 32 μm was performed inside an Ar glovebox.

4.2. Incipient wetness impregnation

To synthesize the W-LNO—$Ni(OH)_2$–5% and W-LNO—NiO–3% or –5% CAMs, an ethanolic solution of WCl_6 (0.126 mol/L) was gradually added to either $Ni(OH)_2$ or NiO, in a ratio of 1:5 of solution to pCAM (i.e., 0.4 mL for 2 g of $Ni(OH)_2$ [equivalent to 1.6 g of NiO]). Of note, NiO was produced from the pCAM by heating at 400 °C for 5 h in an O_2 atmosphere (4 L/h). Both impregnated materials were left to dry in an Ar glovebox and then heated to 400 °C for 5 h in an O_2 atmosphere (4 L/h). Next, $LiOH{\cdot}H_2O$ was added, considering Li:Ni molar ratios of 1.05 and 1.03. As described above, the solids were mixed using a laboratory blender (Kinematica AG), followed by transfer to a ceramic crucible. The calcination conditions were 4 h at 400 °C and 6 h at 700, 750, or 800 °C, with a heating rate of 3 °C/min, in an O_2 atmosphere (4 L/h). Subsequently, sieving to 32 μm was again performed in an Ar glovebox.

4.3. Electrochemical testing

For SSBs, the cold-pressed cathode composites were prepared by blending 69.3 wt.% CAM, 29.7 wt.% Li_6PS_5Cl (NEI Corp.), and 1.0 wt.% Super C65 (TIMCAL Ltd.) under inert conditions via ball milling (FRITSCH planetary mill) at 140 rpm for 30 min. For anode preparation, indium foil (9 mm diameter, 100 μm thick; Changsha Santech Materials Co., Ltd.) and lithium foil (6 mm diameter, 50 μm thick; Albemarle Germany GmbH) were used. A customized cell setup with a PEEK ring of 10 mm inner diameter and two stainless steel dies as current collectors was used. 100 mg of Li_6PS_5Cl was placed in the PEEK ring and compressed at 62 MPa to form the separator layer. Then, about 12 mg of cathode composite was spread on one side of the separator and compressed at 435 MPa for 3 min. Finally, the In/InLi anode was attached on the other side, with the indium foil facing the separator. The assembled

cells were sealed in pouch bags under an Ar atmosphere. The electrochemical performance was tested at different C-rates, with 1C = 190 mA/g_{CAM}, and at 45 °C and 81 MPa using a MACCOR battery cycler. The potential range was set to 2.3–3.7 V vs. In/InLi (approx. 2.9–4.3 V vs. Li^+/Li).

For the preparation of dry-processed cathode sheets, W-LNO—Ni$(OH)_2$–5%, Li_6PS_5Cl, and Super C65 were used in a weight ratio of 70:29:1. The composite was produced by ball milling at 140 rpm for 30 min. For this purpose, a 70 mL zirconia jar containing 10 zirconia balls of 10 mm diameter was used, with the total mass of the composite being about 1 g. Subsequently, it was transferred to a preheated mortar at 80 °C, and 0.5 wt.% polytetrafluorethylene (PTFE, d_{50} = 675 μm; Goodfellow GmbH) was added. The mixture was manually ground for 20 min until PTFE fibrillation occurred and a single flake was formed. This flake was then placed on a glass plate and rolled out using a glass cylinder until the desired thickness (~120 μm) was achieved. The cathode sheet was compacted at 3 N/mm in a dry room with a dew point below −50 °C using a roll press (Sumet Messtechnik). Finally, 9 mm-diameter discs were punched out. The areal loading was about 11 mg_{CAM}/cm^2.

For the preparation of wet-processed cathode sheets, an *o*-xylene slurry containing 68.6:29.4:1.0:1.0 by weight of W-LNO—Ni$(OH)_2$–5%, Li_6PS_5Cl, Super C65, and OPPANOL N 150 polyisobutylene binder (BASF SE) was cast onto 0.03 mm-thick aluminum foil in a dry room with a dew point below −50 °C, followed by vacuum-drying overnight at room temperature. The areal loading was about 10 mg_{CAM}/cm^2.

For LIBs, an N-methyl-pyrrolidone (NMP)-containing slurry was prepared by combining CAM with Super C65 and a polyvinylidene difluoride binder (PVDF, Solef 5130; Solvay) in a weight ratio of 94:3:3. The mixture was cast onto 0.03 mm-thick aluminum foil using a stainless-steel doctor blade with a slit thickness of 140 μm on an Erichsen Coatmaster 510 machine. Subsequently, the cathode was dried overnight under vacuum at 120 °C, calendared at 14 N/mm (Sumet Messtechnik), and cut into circular 13 mm-diameter electrodes. The areal loading was about 9 mg_{CAM}/cm^2. Coin cells (2032) were assembled using the as-prepared electrodes, a glass fiber GF-D separator, LP57 electrolyte (1 M $LiPF_6$ in 3:7 by weight of ethylene carbonate and ethyl methyl carbonate), and a lithium-metal anode in an Ar glovebox. They were crimped at 1 t. The electrochemical performance was tested at 0.5C after five formation cycles at different C-rates (0.05C for two cycles and 0.1C for three cycles), with 1C = 200 mA/g_{CAM}, and at 25 °C. The potential range was set to 3.0–4.3 V vs. Li^+/Li.

4.4. Powder X-ray diffraction

PXRD patterns were collected from the samples on a STADI P (STOE) diffractometer with monochromatic Mo-$K_{\alpha1}$ radiation (λ = 0.7093 Å, 50 kV, 40 mA) using a Mythen 1 K detector (DECTRIS AG). The data acquired were analyzed via GSAS-II. First, Le Bail fitting was performed, followed by background correction applying Chebyshev polynomials. Lattice parameters, zero-shift, and crystallite size (Gaussian and Lorentzian contributions) were refined. In the Rietveld analysis, the Le Bail parameters were fixed first. Debye-Scherrer factors were refined with an absorption correction applied. All parameters were refined in parallel until convergence was achieved.

4.5. Synchrotron XRD

SXRD measurements were performed with a photon energy of 75 keV (λ = 0.165 Å) using beamline ID31 at ESRF (European Synchrotron Radiation Facility) in Grenoble, France. High-resolution diffraction patterns were acquired using a Pilatus CdTe 2M detector (1678 × 1475 pixels with 172 × 172 μm^2 each, sample-to-detector distance of about 1.5 m).

4.6. Scanning electron microscopy

SEM images were obtained on a LEO-1530 microscope (Carl Zeiss AG) equipped with a field-emission source. Energy-dispersive X-ray (EDX) spectroscopy mapping was performed at an acceleration voltage of 20 kV. Samples for cross-sectional analysis were prepared by focused ion beam (FIB) SEM using a Helios 5 CX DualBeam (Thermo Fisher Scientific).

4.7. Scanning transmission electron microscopy

STEM measurements were performed at an accelerating voltage of 300 kV using a probe-corrected Titan Themis Z (Thermo Fisher Scientific) microscope equipped with a SuperX EDX detector. Specimens were prepared by FIB SEM. STEM investigations were performed using high-angle annular dark-field (HAADF) and annular bright-field (ABF) detectors at a camera length of 91 mm and a semi-collection angle of 30 mrad. Electron energy loss spectroscopy (EELS) was performed at a dispersion of 0.3 eV/channel and 1 eV energy resolution.

4.8. Acoustic emission analysis

AE signals were recorded using a differential wideband sensor (125–1000 kHz; MISTRAS Group) placed at the bottom of coin cells. The experimental setup included an inline preamplifier and a data-acquisition system (USB AE Node; MISTRAS Group). The pre-amplifier gain, analog filter, and sampling rate were set at 40 dB, 20–1000 kHz, and 5 MSPS, respectively. The sensor coupling was verified via the pencil lead break test. At least two samples were tested to ensure data reliability. Removal of background noise using the AEwin software (MISTRAS Group) involved excluding hits of fewer than 2 counts and those with peak frequencies below 100 kHz and/or amplitudes below 27 dB.

4.9. Electrochemical impedance spectroscopy

EIS was performed at 45 °C using an SP-300 potentiostat (BioLogic) over a frequency range of 100 mHz to 1 MHz (10 mV perturbation amplitude). Distribution of relaxation times (DRT) analysis was conducted by evaluating the complex impedance data using a discretization method based on radial Gaussian basis functions. The shape factor and regularization parameter were set at 0.5 and $1.0 \cdot 10^{-4}$.

4.10. X-ray photoelectron spectroscopy

Prior to XPS analysis, the solid electrolyte separator was extracted from the pellet stacks. The samples were fixed on a holder using conductive copper tape. To further improve electronic contact, the sample surface was connected to the holder via conductive metal pins. The holder was then transferred to the spectrometer. Both sample preparation and transfer were carried out under inert atmosphere. Measurements were performed on a K-alpha spectrometer (Thermo Fisher Scientific) using a monochromatic, micro-focused Al-K_α X-ray source ($h\nu$ = 1486.6 eV) with 400 μm spot size and pass energy of 50 eV. The Thermo Avantage software (version 6.8.1) was used for data acquisition and processing. Samples were measured with and without charge compensation (electron flood gun with low energy electrons of 8 eV) to identify localized charging effects. Because no shifts in binding energies were observed, only spectra without charge compensation were considered. To ensure reproducibility, three spots were measured on each sample. The spectra were referenced to the hydrocarbon C 1s signal at 285 eV and normalized to the maximum peak height of 1. Shirley-type background and Voigt profiles with 70% Gaussian and 30% Lorentzian contributions were used for peak fitting. The active carbon (sp^2) peak was fitted asymmetrically with a tail mix of 75% and a tail exponent of 0.1. For quantification, the analyzer transmission function and Scofield

sensitivity factors were applied.

4.11. Differential electrochemical mass spectrometry

For *in situ* gas analysis, the SSB cells were prepared similar to the electrochemical testing, except that only indium foil was used as anode. The cells were assembled in a 10 mm-diameter PEEK ring by sequentially pressing the individual components into a pellet, then transferring it into a customized DEMS setup. Galvanostatic cycling was performed at a rate of 0.05C and at 45 °C in a potential window of 2.3–3.7 V vs. In/InLi (without charge-capacity limitation) using a VSP-300 potentiostat (Biologic). To ensure thermal equilibrium and a stable baseline, all cells were held at open-circuit voltage for 6 h prior to cycling. The helium carrier-gas flow (2.5 mL/min, 6.0 purity) was regulated by a mass flow controller (F-201CV-020-RAD-33-Z; Bronkhorst). Gas evolution was examined using a quadrupole mass spectrometer (OmniStar GSD 320 O; Pfeiffer Vacuum GmbH).

CRediT authorship contribution statement

Philip Henkel: Writing – original draft, Visualization, Methodology, Investigation, Formal analysis, Conceptualization. **Ruizhuo Zhang:** Writing – review & editing, Investigation, Formal analysis. **Rajib Sahu:** Writing – review & editing, Investigation, Formal analysis. **Christian Kübel:** Writing – review & editing, Formal analysis. **Jensheer Shamsudeen Seenath:** Writing – review & editing, Investigation, Formal analysis. **Maik Schmitt:** Writing – review & editing, Investigation. **Ulf-Christian Rauska:** Writing – review & editing, Investigation, Formal analysis. **Celine Röder:** Writing – review & editing, Investigation, Formal analysis. **Fabian Jeschull:** Writing – review & editing, Investigation. **Jürgen Janek:** Supervision, Funding acquisition. **Aleksandr Kondrakov:** Supervision, Project administration, Funding acquisition. **Torsten Brezesinski:** Writing – review & editing, Supervision, Project administration, Funding acquisition.

Declaration of competing interest

The authors declare that they have no known competing financial interests or personal relationships that could have appeared to influence the work reported in this paper.

Acknowledgements

This study was supported by BASF SE. The authors acknowledge the support from the Karlsruhe Nano Micro Facility (KNMFi, www.knmf.kit.edu), a Helmholtz research infrastructure at Karlsruhe Institute of Technology (KIT, www.kit.edu). They also thank the Momentum Transfer team for their assistance with the SXRD measurements and J. Drnec for support in using beamline ID31. The measurement setup was developed with funding from the European Union's Horizon 2020 research and innovation program under the STREAMLINE project (grant agreement ID 870313).

Supplementary materials

Supplementary material associated with this article can be found, in the online version, at doi:10.1016/j.ensm.2026.105353.

Data availability

Data will be made available on request.

References

[1] R. Zhang, F. Strauss, L. Jiang, L. Casalena, L. Li, J. Janek, A. Kondrakov, T. Brezesinski, Transition-metal interdiffusion and solid electrolyte poisoning in all-solid-state batteries revealed by cryo-TEM, Chem. Commun. 59 (2023) 4600–4603, https://doi.org/10.1039/D3CC00516J.

[2] J. Janek, W.G. Zeier, A solid future for battery development, Nat. Energy 1 (2016) 16141, https://doi.org/10.1038/nenergy.2016.141.

[3] F. Walther, F. Strauss, X. Wu, B. Mogwitz, J. Hertle, J. Sann, M. Rohnke, T. Brezesinski, J. Janek, The working principle of a Li_2CO_3/$LiNbO_3$ coating on NCM for thiophosphate-based all-solid-state batteries, Chem. Mater. 33 (2021) 2110–2125, https://doi.org/10.1021/acs.chemmater.0c04660.

[4] J. Schnell, T. Günther, T. Knoche, C. Vieider, L. Köhler, A. Just, M. Keller, S. Passerini, G. Reinhart, All-solid-state lithium-ion and lithium metal batteries – paving the way to large-scale production, J. Power Sources 382 (2018) 160–175, https://doi.org/10.1016/j.jpowsour.2018.02.062.

[5] K.H. Park, Q. Bai, D.H. Kim, D.Y. Oh, Y. Zhu, Y. Mo, Y.S. Jung, Design strategies, practical considerations, and new solution processes of sulfide solid electrolytes for all-solid-state batteries, Adv. Energy Mater. 8 (2018) 1800035, https://doi.org/10.1002/aenm.201800035.

[6] A. Banerjee, X. Wang, C. Fang, E.A. Wu, Y.S. Meng, Interfaces and interphases in all-solid-state batteries with inorganic solid electrolytes, Chem. Rev. 120 (2020) 6878–6933, https://doi.org/10.1021/acs.chemrev.0c00101.

[7] C. Wang, R. Yu, S. Hwang, J. Liang, X. Li, C. Zhao, Y. Sun, J. Wang, N. Holmes, R. Li, H. Huang, S. Zhao, L. Zhang, S. Lu, D. Su, X. Sun, Single crystal cathodes enabling high-performance all-solid-state lithium-ion batteries, Energy Storage Mater. 30 (2020) 98–103, https://doi.org/10.1016/j.ensm.2020.05.007.

[8] Y. Ma, R. Zhang, Y. Tang, Y. Ma, J.H. Teo, T. Diemant, D. Goonetilleke, J. Janek, M. Bianchini, A. Kondrakov, T. Brezesinski, Single- to few-layer nanoparticle cathode coating for thiophosphate-based all-solid-state batteries, ACS Nano 16 (2022) 18682–18694, https://doi.org/10.1021/acsnano.2c07314.

[9] Y. Ma, J.H. Teo, F. Walther, Y. Ma, R. Zhang, A. Mazilkin, Y. Tang, D. Goonetilleke, J. Janek, M. Bianchini, T. Brezesinski, Advanced nanoparticle coatings for stabilizing layered Ni-rich oxide cathodes in solid-state batteries, Adv. Funct. Mater. 32 (2022) 2111829, https://doi.org/10.1002/adfm.202111829.

[10] Z. Jiang, S. Li, J. Yang, M. Deng, Z. Lu, Z. Wang, L. Li, F. Wu, C. Yu, Unravelling the stablization effect of flourination on the interface and bulk phase of electrodes in all-solid-state lithium metal batteries, Mater. Today 90 (2025) 31–42, https://doi.org/10.1016/j.mattod.2025.08.019.

[11] B. Nascimento Nunes, L. Karger, R. Zhang, A. Kondrakov, T. Brezesinski, Enhanced cycling performance of the $LiNiO_2$ cathode in Li-ion batteries enabled by Nb-based surface coating, ChemSusChem 18 (2025) e202402202, https://doi.org/10.1002/cssc.202402202.

[12] L. deBiasi, A. Schiele, M. Roca-Ayats, G. Garcia, T. Brezesinski, P. Hartmann, J. Janek, Phase transformation behavior and stability of $LiNiO_2$ cathode material for Li-ion batteries obtained from in situ gas analysis and operando X-ray diffraction, ChemSusChem 12 (2019) 2240–2250, https://doi.org/10.1002/cssc.201900032.

[13] M. Bianchini, M. Roca-Ayats, P. Hartmann, T. Brezesinski, J. Janek, There and back again—the journey of $LiNiO_2$ as a cathode active material, Angew. Chem. Int. Ed. 58 (2019) 10434–10458, https://doi.org/10.1002/anie.201812472.

[14] H. Nguyen, R. Silverstein, A. Zaveri, W. Cui, P. Kurzhals, S. Sicolo, M. Bianchini, K. Seidel, R.J. Clément, Twin boundaries contribute to the first cycle irreversibility of $LiNiO_2$, Adv. Funct. Mater. 34 (2024) 2306168, https://doi.org/10.1002/adfm.202306168.

[15] L. Karger, A. Kondrakov, T. Brezesinski, On the mechanistic understanding of first-cycle capacity loss in polycrystalline and single-crystal layered Ni-rich oxide cathodes for Li-ion batteries, ChemistryEurope 3 (2025) e202500097, https://doi.org/10.1002/ceur.202500097.

[16] L. Karger, S. Korneychuk, W. van den Bergh, S.L. Dreyer, R. Zhang, A. Kondrakov, J. Janek, T. Brezesinski, Seesaw effect of substitutional point defects on the electrochemical performance of single-crystal $LiNiO_2$ cathodes, Chem. Mater. 36 (2024) 1497–1512, https://doi.org/10.1021/acs.chemmater.3c02727.

[17] J. Chen, Y. Yang, Y. Tang, Y. Wang, H. Li, X. Xiao, S. Wang, M.S.D. Darma, M. Etter, A. Missyul, A. Tayal, M. Knapp, H. Ehrenberg, S. Indris, W. Hua, Constructing a thin disordered self-protective layer on the $LiNiO_2$ primary particles against oxygen release, Adv. Funct. Mater. 33 (2023) 2211515, https://doi.org/10.1002/adfm.202211515.

[18] G. Nuroldayeva, T. Umurzak, A. Kireyeva, A. Aishova, O. Mukhan, S.-S. Kim, Z. Bakenov, N. Umirov, A comparative study of bulk and surface W-doped high-Ni cathode materials for lithium-ion batteries, Nanoscale 17 (2025) 8192–8205, https://doi.org/10.1039/D4NR04691A.

[19] A.O. Kondrakov, H. Geßwein, K. Galdina, L. de Biasi, V. Meded, E.O. Filatova, G. Schumacher, W. Wenzel, P. Hartmann, T. Brezesinski, J. Janek, Charge-transfer-induced lattice collapse in Ni-rich NCM cathode materials during delithiation, J. Phys. Chem. C 121 (2017) 24381–24388, https://doi.org/10.1021/acs.jpcc.7b06598.

[20] P. Kurzhals, F. Riewald, M. Bianchini, H. Sommer, H.A. Gasteiger, J. Janek, The $LiNiO_2$ cathode active material: a comprehensive study of calcination conditions and their correlation with physicochemical properties. Part I. Structural chemistry, J. Electrochem. Soc. 168 (2021) 110518, https://doi.org/10.1149/1945-7111/ac33e5.

[21] J. Xu, E. Hu, D. Nordlund, A. Mehta, S.N. Ehrlich, X.-Q. Yang, W. Tong, Understanding the degradation mechanism of lithium nickel oxide cathodes for Li-ion batteries, ACS Appl. Mater. Interfaces 8 (2016) 31677–31683, https://doi.org/10.1021/acsami.6b11111.

[22] C.S. Yoon, D.-W. Jun, S.-T. Myung, Y.-K. Sun, Structural stability of $LiNiO_2$ cycled above 4.2 V, ACS Energy Lett. 2 (2017) 1150–1155, https://doi.org/10.1021/acsenergylett.7b00304.

[23] H.-H. Ryu, K.-J. Park, C.S. Yoon, Y.-K. Sun, Capacity fading of Ni-rich Li $[Ni_xCo_yMn_{1-x-y}]O_2$ ($0.6 \leq x \leq 0.95$) cathodes for high-energy-density lithium-ion batteries: bulk or surface degradation? Chem. Mater. 30 (2018) 1155–1163, https://doi.org/10.1021/acs.chemmater.7b05269.

[24] M. Kim, L. Zou, S.-B. Son, I.D. Bloom, C. Wang, G. Chen, Improving $LiNiO_2$ cathode performance through particle design and optimization, J. Mater. Chem. A 10 (2022) 12890–12899, https://doi.org/10.1039/D2TA02492F.

[25] S. Yin, W. Deng, J. Chen, X. Gao, G. Zou, H. Hou, X. Ji, Fundamental and solutions of microcrack in Ni-rich layered oxide cathode materials of lithium-ion batteries, Nano Energy 83 (2021) 105854, https://doi.org/10.1016/j.nanoen.2021.105854.

[26] L. Wen, F. Cheng, X. Wang, X. Zeng, T. Wang, L. Li, Y. Hu, Q. Yu, W. Lu, Recent advances of cobalt-free and nickel-rich cathode materials for lithium-ion batteries, Energy Mater. 4 (2024) 4, https://doi.org/10.20517/energymater.2024.08.

[27] H. Wei, L. Tang, Y. Huang, Z. Wang, Y. Luo, Z. He, C. Yan, J. Mao, K. Dai, J. Zheng, Comprehensive understanding of Li/Ni intermixing in layered transition metal oxides, Mater. Today 51 (2021) 365–392, https://doi.org/10.1016/j.mattod.2021.09.013.

[28] A. Manthiram, J.C. Knight, S. Myung, S. Oh, Y. Sun, Nickel-rich and lithium-rich layered oxide cathodes: progress and perspectives, Adv. Energy Mater. 6 (2016) 1501010, https://doi.org/10.1002/aenm.201501010.

[29] H. Arai, S. Okada, H. Ohtsuka, M. Ichimura, J. Yamaki, Characterization and cathode performance of $Li_{1-x}Ni_{1+x}O_2$ prepared with the excess lithium method, Solid State Ion. 80 (1995) 261–269, https://doi.org/10.1016/0167-2738(95)00144-U.

[30] U.-H. Kim, D.-W. Jun, K.-J. Park, Q. Zhang, P. Kaghazchi, D. Aurbach, D.T. Major, G. Goobes, M. Dixit, N. Leifer, C.M. Wang, P. Yan, D. Ahn, K.-H. Kim, C.S. Yoon, Y.-K. Sun, Pushing the limit of layered transition metal oxide cathodes for high-energy density rechargeable Li ion batteries, Energy Environ. Sci. 11 (2018) 1271–1279, https://doi.org/10.1039/C8EE00227D.

[31] M. Dalkilic, A. Schmidt, T.D. Schladt, P. Axmann, M. Wohlfahrt-Mehrens, M. Lindén, W-doping of dense NMC811 hydroxide through wet-impregnation and its impact on crystal structure, phase transition related gas evolution and electrochemical performance at elevated upper cut-off voltage, J. Electrochem. Soc. 169 (2022) 120501, https://doi.org/10.1149/1945-7111/aca360.

[32] U.-H. Kim, G.-T. Park, B.-K. Son, G.W. Nam, J. Liu, L.-Y. Kuo, P. Kaghazchi, C. S. Yoon, Y.-K. Sun, Heuristic solution for achieving long-term cycle stability for Ni-rich layered cathodes at full depth of discharge, Nat. Energy 5 (2020) 860–869, https://doi.org/10.1038/s41560-020-00693-6.

[33] H.H. Sun, U.-H. Kim, J.-H. Park, S.-W. Park, D.-H. Seo, A. Heller, C.B. Mullins, C. S. Yoon, Y.-K. Sun, Transition metal-doped Ni-rich layered cathode materials for durable Li-ion batteries, Nat. Commun. 12 (2021) 6552, https://doi.org/10.1038/s41467-021-26815-6.

[34] C. Geng, D. Rathore, D. Heino, N. Zhang, I. Hamam, N. Zaker, G.A. Botton, R. Omessi, N. Phattharasupakun, T. Bond, C. Yang, J.R. Dahn, Mechanism of action of the tungsten dopant in $LiNiO_2$ positive electrode materials, Adv. Energy Mater. 12 (2022) 2103067, https://doi.org/10.1002/aenm.202103067.

[35] Z. Zhu, A. Gao, Y. Liang, F. Yi, T. Meng, J. Ling, J. Hao, D. Shu, Dual-functional tungsten boosted lithium-ion diffusion and structural integrity of $LiNi_{0.8}Co_{0.1}Mn_{0.1}O_2$ cathodes for high performance lithium-ion batteries, ACS Sustain. Chem. Eng. 10 (2022) 50–60, https://doi.org/10.1021/acssuschemeng.1c04076.

[36] H.-H. Ryu, G.-T. Park, C.S. Yoon, Y.-K. Sun, Suppressing detrimental phase transitions *via* tungsten doping of $LiNiO_2$ cathode for next-generation lithium-ion batteries, J. Mater. Chem. A 7 (2019) 18580–18588, https://doi.org/10.1039/C9TA06402H.

[37] D. Rathore, C. Geng, N. Zaker, I. Hamam, Y. Liu, P. Xiao, G.A. Botton, J. Dahn, C. Yang, Tungsten infused grain boundaries enabling universal performance enhancement of Co-free Ni-rich cathode materials, J. Electrochem. Soc. 168 (2021) 120514, https://doi.org/10.1149/1945-7111/ac3c26.

[38] B. Luo, B. Jiang, P. Peng, J. Huang, J. Chen, M. Li, L. Chu, Y. Li, Improving the electrochemical performance of $LiNi_{1/3}Co_{1/3}Mn_{1/3}O_2$ cathode material via tungsten modification, Electrochim. Acta 297 (2019) 398–405, https://doi.org/10.1016/j.electacta.2018.11.202.

[39] N. Park, S. Kim, M. Kim, S. Han, D. Kim, M. Kim, Y. Sun, Mechanism of doping with high-valence elements for developing Ni-rich cathode materials, Adv. Energy Mater. 13 (2023) 2301530, https://doi.org/10.1002/aenm.202301530.

[40] N. Yoshinaga, S. Kumakura, K. Kubota, T. Horiba, S. Komaba, Lithium magnesium tungstate solid as an additive into $Li(Ni_{1/3}Mn_{1/3}Co_{1/3})O_2$ electrodes for Li-ion batteries, J. Electrochem. Soc. 166 (2019) A5430–A5436, https://doi.org/10.1149/2.0581903jes.

[41] Y.-Q. Sun, W. Fu, Y.-X. Hu, J. Vaughan, L.-Z. Wang, The role of tungsten-related elements for improving the electrochemical performances of cathode materials in lithium ion batteries, Tungsten 3 (2021) 245–259, https://doi.org/10.1007/s42864-021-00083-9.

[42] G. Shang, Y. Tang, Y. Lai, J. Wu, X. Yang, H. Li, C. Peng, J. Zheng, Z. Zhang, Enhancing structural stability unto 4.5 V of Ni-rich cathodes by tungsten-doping for lithium storage, J. Power Sources 423 (2019) 246–254, https://doi.org/10.1016/j.jpowsour.2019.03.072.

[43] D. Becker, M. Börner, R. Nölle, M. Diehl, S. Klein, U. Rodehorst, R. Schmuch, M. Winter, T. Placke, Surface modification of Ni-rich $LiNi_{0.8}Co_{0.1}Mn_{0.1}O_2$ cathode material by tungsten oxide coating for improved electrochemical performance in lithium-ion batteries, ACS Appl. Mater. Interfaces 11 (2019) 18404–18414, https://doi.org/10.1021/acsami.9b02889.

[44] M. Dalkilic, A. Schmidt, T.D. Schladt, P. Axmann, M. Wohlfahrt-Mehrens, M. Lindén, Synthesis of tantalum doped NMC811 and its impact on crystal structure and electrochemical performance at higher upper cut-off voltage, J. Electrochem. Soc. 169 (2022) 090504, https://doi.org/10.1149/1945-7111/ac8a1b.

[45] S.L. Dreyer, P. Kurzhals, S.B. Seiffert, P. Müller, A. Kondrakov, T. Brezesinski, J. Janek, The effect of doping process route on $LiNiO_2$ cathode material properties, J. Electrochem. Soc. 170 (2023) 060530, https://doi.org/10.1149/1945-7111/acdd21.

[46] S. Eskandari, G. Tate, N.R. Leaphart, J.R. Regalbuto, Nanoparticle synthesis via electrostatic adsorption using incipient wetness impregnation, ACS Catal. 8 (2018) 10383–10391, https://doi.org/10.1021/acscatal.8b03435.

[47] P. Munnik, P.E. De Jongh, K.P. de Jong, Recent developments in the synthesis of supported catalysts, Chem. Rev. 115 (2015) 6687–6718, https://doi.org/10.1021/cr500486u.

[48] F. Pinna, Supported metal catalysts preparation, Catal. Today 41 (1998) 129–137, https://doi.org/10.1016/S0920-5861(98)00043-1.

[49] C.B. Lim, Y.J. Park, Precursor-based surface modification of cathodes using Ta and W for sulfide-based all-solid-state batteries, Sci. Rep. 10 (2020) 10501, https://doi.org/10.1038/s41598-020-67493-6.

[50] F. Liu, R. Kirchheim, Comparison between kinetic and thermodynamic effects on grain growth, Thin Solid Films 466 (2004) 108–113, https://doi.org/10.1016/j.tsf.2004.03.018.

[51] E. McCalla, G.H. Carey, J.R. Dahn, Lithium loss mechanisms during synthesis of layered $Li_xNi_{2-x}O_2$ for lithium ion batteries, Solid State Ion. 219 (2012) 11–19, https://doi.org/10.1016/j.ssi.2012.05.007.

[52] Y.S. Byeon, H.B. Lee, Y. Hong, H. Kim, Y.-J. Kim, W. Cho, M.-S. Park, Cation-deficient Li_xWO_3 surface coating on Ni-rich cathodes materials for lithium-ion batteries, ACS Appl. Mater. Interfaces 17 (2025) 9322–9331, https://doi.org/10.1021/acsami.4c18935.

[53] W. Lee, S. Muhammad, C. Sergey, H. Lee, J. Yoon, Y. Kang, W. Yoon, Advances in the cathode materials for lithium rechargeable batteries, Angew. Chem. Int. Ed. 59 (2020) 2578–2605, https://doi.org/10.1002/anie.201902359.

[54] C. Delmas, M. Ménétrier, L. Croguennec, I. Saadoune, A. Rougier, C. Pouillerie, G. Prado, M. Grüne, L. Fournès, An overview of the $Li(Ni,M)O_2$ systems: syntheses, structures and properties, Electrochim. Acta 45 (1999) 243–253, https://doi.org/10.1016/S0013-4686(99)00208-X.

[55] V. Bianchi, Synthesis, structural characterization and magnetic properties of quasistoichiometric $LiNiO_2$, Solid State Ion. 140 (2001) 1–17, https://doi.org/10.1016/S0167-2738(01)00706-8.

[56] H. Arai, Reversibility of $LiNiO_2$ cathode, Solid State Ion. 95 (1997) 275–282, https://doi.org/10.1016/S0167-2738(96)00598-X.

[57] L. Hou, Q. Liu, X. Chen, Q. Yang, D. Mu, L. Li, F. Wu, R. Chen, In-depth understanding of the deterioration mechanism and modification engineering of high energy density Ni-rich layered lithium transition-metal oxide cathode for lithium-ion batteries, Chem. Eng. J. 465 (2023) 142946, https://doi.org/10.1016/j.cej.2023.142946.

[58] G.-T. Park, D.R. Yoon, U.-H. Kim, B. Namkoong, J. Lee, M.M. Wang, A.C. Lee, X. W. Gu, W.C. Chueh, C.S. Yoon, Y.-K. Sun, Ultrafine-grained Ni-rich layered cathode for advanced Li-ion batteries, Energy Environ. Sci. 14 (2021) 6616–6626, https://doi.org/10.1039/D1EE02898G.

[59] U.-H. Kim, J.-H. Kim, J.-Y. Hwang, H.-H. Ryu, C.S. Yoon, Y.-K. Sun, Compositionally and structurally redesigned high-energy Ni-rich layered cathode for next-generation lithium batteries, Mater. Today 23 (2019) 26–36, https://doi.org/10.1016/j.mattod.2018.12.004.

[60] U. Kim, H. Ryu, J. Kim, R. Mücke, P. Kaghazchi, C.S. Yoon, Y. Sun, Microstructure-controlled Ni-rich cathode material by microscale compositional partition for next-generation electric vehicles, Adv. Energy Mater. 9 (2019) 1803902, https://doi.org/10.1002/aenm.201803902.

[61] J. Wang, Y. Yan, Z. Zhao, J. Li, G. Luo, D. Deng, W. Peng, M. Dong, Z. Wang, G. Yan, H. Guo, H. Duan, L. Li, S. Feng, X. Ou, J. Zheng, J. Wang, Promoting homogeneous tungsten doping in $LiNiO_2$ through a grain boundary phase induced by excessive lithium, Adv. Powder Mater. 4 (2025) 100248, https://doi.org/10.1016/j.apmate.2024.100248.

[62] Y. Huang, C. Li, K. Zhang, Y. Tang, W. Tu, Y. Tian, J. Wang, Y. Yan, Y. Chen, Y. Zou, L. Li, B. Zhang, J. Bao, C. Ding, Y. Wang, T. Qiu, X. Sun, Y. Qiao, S. Sun, How does the precursor influence the Li-rich layered oxide cathode? Angew. Chem. Int. Ed. 64 (2025) e18277 https://doi.org/10.1002/anie.202518277.

[63] R. Zhang, A. Kondrakov, J. Janek, T. Brezesinski, Interfacial anode kinetics and its influence on cycling performance of sulfide solid-state batteries, ACS Nano 20 (2026) 1225–1237, https://doi.org/10.1021/acsnano.5c17276.

[64] R. Zhang, A. Kondrakov, J. Janek, T. Brezesinski, Timescale identification of electrochemical processes in all-solid-state batteries using an advanced three-electrode cell setup, Energy Storage Mater. 75 (2025) 104000, https://doi.org/10.1016/j.ensm.2025.104000.

[65] W. Zhao, R. Zhang, F. Ren, L. Karger, S.L. Dreyer, J. Lin, Y. Ma, Y. Cheng, A.S. Pal, M. Velazquez-Rizo, A. Ahmadian, Z. Zhang, P. Müller, J. Janek, Y. Yang, A. Kondrakov, T. Brezesinski, Protective coating of single-crystalline Ni-rich cathode enables fast charging in all-solid-state batteries, ACS Nano 19 (2025) 8595–8607, https://doi.org/10.1021/acsnano.4c14322.

[66] R. Zhang, S. Payandeh, Y. Ma, D. Goonetilleke, Y. Tang, A. Kondrakov, J. Janek, T. Brezesinski, Compromise between energy density and stability: proper capacity balancing enables high-performance solid-state batteries, Energy Storage Mater. 87 (2026) 105045, https://doi.org/10.1016/j.ensm.2026.105045.

[67] Y. Lu, C.-Z. Zhao, J.-Q. Huang, Q. Zhang, The timescale identification decoupling complicated kinetic processes in lithium batteries, Joule 6 (2022) 1172–1198, https://doi.org/10.1016/j.joule.2022.05.005.

[68] P. Yan, J. Zheng, M. Gu, J. Xiao, J.-G. Zhang, C.-M. Wang, Intragranular cracking as a critical barrier for high-voltage usage of layer-structured cathode for lithium-ion batteries, Nat. Commun. 8 (2017) 14101, https://doi.org/10.1038/ncomms14101.
[69] N. Wu, H. Wu, W. Yuan, S. Liu, J. Liao, Y. Zhang, Facile synthesis of one-dimensional $LiNi_{0.8}Co_{0.15}Al_{0.05}O_2$ microrods as advanced cathode materials for lithium ion batteries, J. Mater. Chem. A 3 (2015) 13648–13652, https://doi.org/10.1039/C5TA02767E.
[70] D.J. Miller, C. Proff, J.G. Wen, D.P. Abraham, J. Bareño, Observation of microstructural evolution in Li battery cathode oxide particles by in situ electron microscopy, Adv. Energy Mater. 3 (2013) 1098–1103, https://doi.org/10.1002/aenm.201300015.
[71] S. An, L. Karger, P. Müller, J. Lin, S. Vasala, V. Baran, S.L. Dreyer, R. Zhang, F. Ulusoy, A. Kondrakov, J. Janek, T. Brezesinski, Exploring calcium pillaring of O3-type $NaNi_{0.9}Ti_{0.1}O_2$ cathodes to advance Na-ion battery technology, Chem. Eng. J. 509 (2025) 160939, https://doi.org/10.1016/j.cej.2025.160939.
[72] S.L. Dreyer, R. Zhang, J. Wang, A. Kondrakov, Q. Wang, T. Brezesinski, J. Janek, The effect of configurational entropy on acoustic emission of P2-type layered oxide cathodes for sodium-ion batteries, J. Phys. Energy 5 (2023) 035002, https://doi.org/10.1088/2515-7655/acd41a.
[73] S. Schweidler, M. Bianchini, P. Hartmann, T. Brezesinski, J. Janek, The sound of batteries: an operando acoustic emission study of the $LiNiO_2$ cathode in Li-ion cells, Batter. Supercaps 3 (2020) 1021–1027, https://doi.org/10.1002/batt.202000099.
[74] F. Walther, R. Koerver, T. Fuchs, S. Ohno, J. Sann, M. Rohnke, W.G. Zeier, J. Janek, Visualization of the interfacial decomposition of composite cathodes in argyrodite-based all-solid-state batteries using time-of-flight secondary-ion mass spectrometry, Chem. Mater. 31 (2019) 3745–3755, https://doi.org/10.1021/acs.chemmater.9b00770.
[75] Z. Wu, L. Du, T. Yang, H. Zhang, W. Zhang, Y. Xia, R. Fang, H. Huang, Y. Gan, X. Xia, X. He, X. Tao, J. Zhang, Lithium difluorophosphate additive engineering enabling stable cathodic interface for high-performance sulfide-based all-solid-state lithium battery, Energy Environ. Mater. 8 (2025) e12871, https://doi.org/10.1002/eem2.12871.
[76] Y. Ma, J.H. Teo, D. Kitsche, T. Diemant, F. Strauss, Y. Ma, D. Goonetilleke, J. Janek, M. Bianchini, T. Brezesinski, Cycling performance and limitations of $LiNiO_2$ in solid-state batteries, ACS Energy Lett. 6 (2021) 3020–3028, https://doi.org/10.1021/acsenergylett.1c01447.
[77] J.F. Moulder, J. Chastain (Eds.), *Handbook of X-Ray Photoelectron Spectroscopy: A Reference Book of Standard Spectra For Identification and Interpretation of XPS Data*, Update., Perkin-Elmer Corporation, Eden Prairie, Minn, 1992.
[78] R. Jung, M. Metzger, F. Maglia, C. Stinner, H.A. Gasteiger, Chemical versus electrochemical electrolyte oxidation on NMC111, NMC622, NMC811, LNMO, and conductive carbon, J. Phys. Chem. Lett. 8 (2017) 4820–4825, https://doi.org/10.1021/acs.jpclett.7b01927.
[79] R. Jung, M. Metzger, F. Maglia, C. Stinner, H.A. Gasteiger, Oxygen release and its effect on the cycling stability of $LiNi_xMn_yCo_zO_2$ (NMC) cathode materials for Li-ion batteries, J. Electrochem. Soc. 164 (2017) A1361–A1377, https://doi.org/10.1149/2.0021707jes.
[80] B. Rowden, N. Garcia-Araez, A review of gas evolution in lithium ion batteries, Energy Rep. 6 (2020) 10–18, https://doi.org/10.1016/j.egyr.2020.02.022.
[81] T. Bartsch, F. Strauss, T. Hatsukade, A. Schiele, A.-Y. Kim, P. Hartmann, J. Janek, T. Brezesinski, Gas evolution in all-solid-state battery cells, ACS Energy Lett. 3 (2018) 2539–2543, https://doi.org/10.1021/acsenergylett.8b01457.
[82] S.E. Renfrew, B.D. McCloskey, Residual lithium carbonate predominantly accounts for first cycle CO_2 and CO outgassing of Li-stoichiometric and Li-rich layered transition-metal oxides, J. Am. Chem. Soc. 139 (2017) 17853–17860, https://doi.org/10.1021/jacs.7b08461.
[83] A.-Y. Kim, F. Strauss, T. Bartsch, J.H. Teo, T. Hatsukade, A. Mazilkin, J. Janek, P. Hartmann, T. Brezesinski, Stabilizing effect of a hybrid surface coating on a Ni-rich NCM cathode material in all-solid-state batteries, Chem. Mater. 31 (2019) 9664–9672, https://doi.org/10.1021/acs.chemmater.9b02947.